ACTA MATERIALIA TRANSYLVANICA

Material Sciences Publications

Volume 8, Issue 1



ERDÉLYI MÚZEUM-EGYESÜLET Kolozsvár 2025 A folyóirat megjelenését támogatta a Communitas Alapítvány, a Magyar Tudományos Akadémia, a Bethlen Gábor Alapkezelő Zrt. és az EME Műszaki Tudományok Szakosztálya / The publication of this magazine was supported by the Communitas Foundation, by the Hungarian Academy of Sciences, by the Bethlen Gábor Fund and by the TMS – Department of Engineering Sciences.









Főszerkesztő / Editor-in-Chief: Bitay Enikő

Nemzetközi Tanácsadó testület / International Editorial Advisory Board:

Prof. Biró László Péter, MTA Energiatudományi Kutatóközpont, Budapest, Magyarország

Prof. emer. B. Nagy János, University of Namur, Namur, Belgium

Prof. Czigány Tibor, Budapesti Műszaki és Gazdaságtudományi Egyetem, Budapest, Magyarország

Prof. Diószegi Attila, Jönköping University, Jönköping, Svédország

Dobránszky János, HUN-REN-BME Kompozittechnológiai Kutatócsoport, Budapest, Magyarország Prof. Dusza János, Institute of Materials Research of Slovak Academy of Sciences, Kassa, Szlovákia

Prof. Kaptay György, Miskolci Egyetem, Miskolc, Magyarország

Dr. Kolozsváry Zoltán, Plasmaterm Rt., Marosvásárhely, Románia

Prof. Mertinger Valéria, Miskolci Egyetem, Miskolc, Magyarország

Prof. Porkoláb Miklós, Massachusetts Institute of Technology, Cambridge, MA, USA

Prof. Réger Mihály, Óbudai Egyetem, Budapest, Magyarország Prof. emer. Réti Tamás, Óbudai Egyetem, Budapest, Magyarország

Prof. emer. Roósz András, Miskolci Egyetem, Miskolc, Magyarország

Dr. Spenik Sándor, Ungvári Nemzeti Egyetem, Ungvár, Ukrajna

Prof. Zsoldos Ibolya, Széchenyi István Egyetem, Győr, Magyarország

Lapszámszerkesztők / Editorial Board:

Dobránszky János, HUN-REN-BME Kompozittechnológiai Kutatócsoport, Budapest, Magyarország Csavdári Alexandra, Babes-Bolyai Tudományegyetem, Kolozsvár, Románia Gergely Attila, Sapientia Erdélyi Magyar Tudományegyetem, Marosvásárhely, Románia Kovács Tünde, Óbudai Egyetem, Budapest, Magyarország

Kiadó / Publisher: Erdélyi Múzeum-Egyesület

Felelős kiadó / Responsible publisher: Biró Annamária

Olvasószerkesztő / Proofreader: Szenkovics Enikő (magyar), David Speight (English)

Szerkesztőségi titkár / Editorial secretary: Kisfaludi-Bak Zsombor

Borítótery / Cover: Könczey Elemér

Nyomdai munkálatok / Printed at: F&F International Kft., Gyergyószentmiklós

Copyright © a szerzők / the authors, EME/ TMS 2024

ISSN 2601-1883, ISSN-L 2601-1883

DOI: 10.33923/amt-2025-01

A folyóirat honlapja: https://www.eme.ro/publication-hu/acta-mat/mat-main.htm The journal website: https://www.eme.ro/publication/acta-mat/mat-main.htm

Az Acta Materialia Transylvanica. Anyagtudományi Közlemények az Erdélyi Múzeum-Egyesület (EME) Műszaki Tudományok Szakosztályának folyóirata, amely az anyagtudományok területéről közöl tudományos közleményeket: szakcikkeket, összefoglalókat (szemléket), tanulmányokat. A folyóirat célja összképet adni kiemelten a Kárpát-medencei kutatási irányokról, tudományos eredményeiről, s ezt széles körben terjeszteni is. A folyóirat az EME felvállalt céljaihoz híven a magyar szaknyelv ápolását is támogatja, így a nyomtatott folyóirat magyar nyelven jelenik meg, mely az Erdélyi digitális adattárban elérhető (https://eda.eme.ro/handle/10598/30356). A széles körű nemzetközi terjesztés érdekében a folyóirat teljes angol nyelvű változatát is közzétesszük.

Acta Materiala Transylvanica – Material Sciences Publications – is a journal of the Technical Sciences Department of the Transvlvanian Museum Society, publishing scientific papers, issues, reviews and studies in the field of material sciences. Its mission is to provide and disseminate a comprehensive picture focusing on research trends and scientific results in the Carpathian basin. In accordance with the general mission of the Transylvanian Museum Society it aims to support specialized literature in Hungarian. The printed version of the journal is published in Hungarian and is available in the Transylvanian Digital Database (https://eda.eme.ro/handle/10598/30356). However, we would like to spread it internationally, therefore the full content of the journal will also be available in English.

Tartalom / Content

BOGNÁR ADRIÁN, KUN KRISZTIÁN, ZSIDAI LÁSZLÓ	1
A technológiai paraméterek hatása PolyJet eljárással előállított próbatestek mechanikai tulajdonságaira	
Effect of Technological Parameters on the Mechanical Properties of Test Specimens Produced by Polyjet Technology	
GERBOVITS DITTA ADRIENN, NAGY ROLAND, PUSKÁS SÁNDOR	8
Környezetbarát tenzidek kőolaj-kihozatali célra való felhasználhatóságának vizsgálata Investigation of the Applicability of Environmentally Friendly Surfactants for Oil Recovery	
KÁNTOR JÓZSEF, GERGELY ATTILA LEVENTE	13
Szálpaplanok előállítása újrahasznosított PET-palackból	
Production of Fibre Mats from Recycled PET Bottles	
KERTÉSZ OLIVÉR GÁBOR, TÓTH LÁSZLÓ	17
UNIMAX szerszámacél tulajdonságainak javítása felületbevonatolással	
Improving the Properties of UNIMAX Tool Steel by Surface Coating	
KOZÁK EMESE, KOVÁCS ZSOLT FERENC	23
A szerszám fejlesztése alumíniumötvözetek kavaró dörzshegesztéséhez	
Tool Development for Friction Stir Welding of Aluminium Alloys	
MÉSZÁROS BÉLA, FÁBIÁN ENIKŐ RÉKA	28
Különböző felületi kialakításokra gyakorolt hatása a lézeres felületedzésnek 1.2379 szerszámacél esetén	
Effect of Laser Surface Hardening on Different Surface Designs in the case of 1.2379 Tool Steel	
SIMON VIRÁG, VARBAI BALÁZS, PUSKÁS ZSOLT	34
A kitöltési tényező és a lézernyaláb lengetésének hatása kézi lézeres hegesztés esetén	
The Effects of the Laser Pulse Duty and the Wobble in Case of Manual Laser Welding	

ZENDI DORINA, TÁRKÁNYI SÁNDOR, KÓSA BALÁZS	38
Fenntarthatóság rétegről rétegre: Liapor- és cellulóz-alapú hőszigetelés kombinációja homlokzati falpanelben	
Sustainability Layer by Layer: Combining Liapor and Cellulose-Based Insulation in a Facade Wall Panel	
ZOVÁK BENEDEK, KEMÉNY ALEXANDRA, ORBULOV IMRE NORBERT	43
Alternatív eljárás irányított szállal erősített szintaktikus fémhabok gyártására	
An Alternative Process for the Production of Oriented Fibre Reinforced Syntactic Metal Foams	
AMIUL ALAM MD, SCHRAMKÓ MÁRTON, KOVÁCS TÜNDE ANNA	47
A szorítónyomás hatása nikkelbevonatos rézlemez és alumíniumlemez között ultrahangos hegesztés közben	
Effect of Welding Pressure During Ultrasonic Welding Between Nickel-Plated Copper and Aluminium Sheets	



Acta Materialia Transylvanica 8/1. (2025) 1–7.

DOI: Hungarian: https://doi.org/10.33923/amt-2025-01-01

English: https://doi.org/10.33924/amt-2025-01-01



Effect of Technological Parameters on the Mechanical Properties of Test Specimens Produced by Polyjet Technology

Adrián BOGNÁR, 1 Krisztián KUN, 2 László ZSIDAI 3

- ¹ John von Neumann University, GAMF Faculty of Engineering and Computer Science, Department of Innovative Vehicles and Materials, Kecskemét, Hungary, bognar.adrian@nje.hu
- ² John von Neumann University, GAMF Faculty of Engineering and Computer Science, Department of Innovative Vehicles and Materials, Kecskemét, Hungary.
- ³ Hungarian University of Agriculture and Life Sciences, Szent István Campus, Institute of Technology, Department of Materials Science and Engineering Processes, Gödöllő, Hungary.

Abstract

The expansion of additive manufacturing technologies enables the rapid and efficient production of parts with complex geometries, making them increasingly important in the production of functional prototypes and finished products. To ensure the reliable performance of these parts, it is essential to optimize the printing parameters and analyze the material properties of the printed parts. In this study, the thermomechanical properties of 3D printed test specimens produced by PolyJet technology were analysed, with a particular focus on the glass transition temperature and the loss factor. The investigation concentrated on the influence of printing orientation and layer thickness, as these key parameters affect the mechanical behaviour of the finished parts.

Keywords: additive manufacturing, PolyJet technology, thermomechanical properties, layer thickness.

1. Introduction

The mechanical properties of test specimens produced using PolyJet technology, such as tensile strength, elongation at break, and elastic modulus, significantly depend on the printing orientation and layer thickness. Tensile tests indicate that variations in printing direction and layer thickness fundamentally influence the mechanical behavior of the test specimens. Additionally, printing orientation affects hardness and glass transition temperature. Dynamic mechanical thermal analysis (DMTA) tests show that the values of complex elastic modulus and loss factor are orientation-dependent. [1] Furthermore, mechanical differences between various materials can also be observed, which change depending on printing parameters, facilitating the fine-tuning of properties required for specific applications.

1.1. Effect of printing orientation on mechanical properties

During the investigation of the mechanical properties of test specimens manufactured using

the PolyJet process, the authors determined that the material exhibits anisotropic behavior. Their study found that within the same plane, changes in orientation did not result in significant differences in the elastic modulus. However, when comparing different build planes, tensile strength and elongation at break showed substantial variations. It was observed that specimens printed in a vertical orientation exhibited increased tensile strength but decreased elongation at break, whereas specimens printed in a horizontal orientation displayed the opposite trend. Changing the layer thickness did not affect the results for horizontally printed specimens but had an impact on the mechanical properties of vertically printed ones. In configurations parallel to the build direction, tensile strength significantly decreased compared to other orientations, reinforcing the anisotropic nature of the material [2].

A separate study using bending tests reached similar conclusions when comparing test specimens produced with different printing orientations. The results showed that specimens manufactured in the Y direction exhibited the highest flexural strength. For rigid materials, the lowest values were observed in the Z direction, whereas for more flexible materials, the lowest flexural strength was recorded in the X direction. Examination of the flexural modulus indicated that the Y orientation yielded more favorable results compared to the X direction, while in the Z direction, the modulus decreased with increasing material flexibility [3].

1.2. The effect of printing orientation and layer thickness on the glass transition temperature

The aim of the research was to investigate the viscoelastic and thermomechanical properties of test specimens printed using PolyJet technology under different printing parameters. In the first experiment, the researchers examined the effect of layer thickness and printing orientation on the glass transition temperature. According to the results, the highest glass transition temperature was observed in the X orientation, while the lowest was in the Y orientation, with a difference of approximately 20°C. Printing with a greater layer thickness resulted in a higher glass transition temperature [4].

1.3. Effect of material quality and printing orientation on the complex elastic modulus and loss factor

In this study, the variation of the complex elastic modulus of PolyJet-manufactured specimens was investigated as a function of in-plane orientation and testing configuration. The results showed no significant difference between horizontal and vertical printing; however, tensile testing yielded higher dynamic modulus values, while bending tests exhibited a higher loss factor. Additionally, the complex modulus and loss factor of different materials were examined. For stiffer materials, the elastic modulus varied by three orders of magnitude with increasing frequency, whereas for more flexible materials, this change was more than fourfold [5, 6].

Based on the reviewed literature sources, it is possible to identify the parameters that influence the mechanical properties of the manufactured parts. The studies clearly indicate that different printing orientations and layer thickness settings affect the mechanical characteristics of the test specimens. Additionally, the quality of the material used plays a key role in the obtained results.

2. Materials and methods

The aim of the present study is to investigate the glass transition temperature of the specimens printed using the PolyJet process, taking into account different layer thicknesses and printing orientations. In the experiment, the material quality remains constant, and its effect is not examined in the article.

2.1. Test specimens

The test specimens were printed in three different orientations: XYZ (A), XZY (B), ZXY (C) (Fig. 1).

The research results showed that printing orientation influenced the mechanical properties; however, the effect of further in-plane arrangements was negligible. The classification and naming of the test specimens are shown in **Table 1**. The layer thickness can be adjusted in parallel with the printing speed, so the chosen settings were (High Speed: HS) and (High Quality: HQ.

For the DMTA tests, rectangular specimens are required, and their dimensions were selected based on the measurement fixture used. The determined dimensions are 35×10×3 mm. The modeling of the specimens and their export to STL format were performed using Autodesk Fusion 360 software.

Table 1. Grouping and naming of test specimens

Orientation	High speed (HS)	High Quality (HQ)
XYZ (A)	HSA	HQA
XZY (B)	HSB	HQB
ZXY (C)	HSC	нос

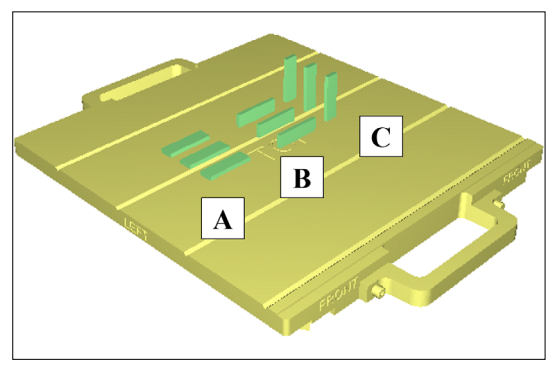


Fig. 1. Test specimen arrangement in the Objet Studio slicing software

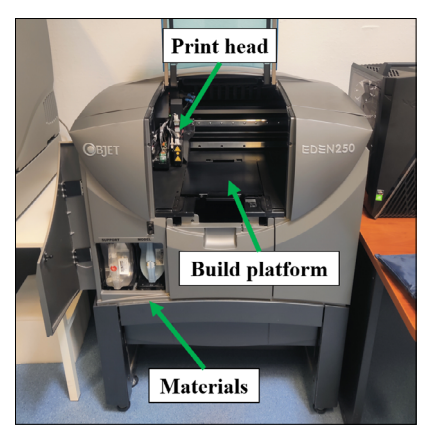


Fig. 2. Objet Eden 250 PolyJet 3D printer

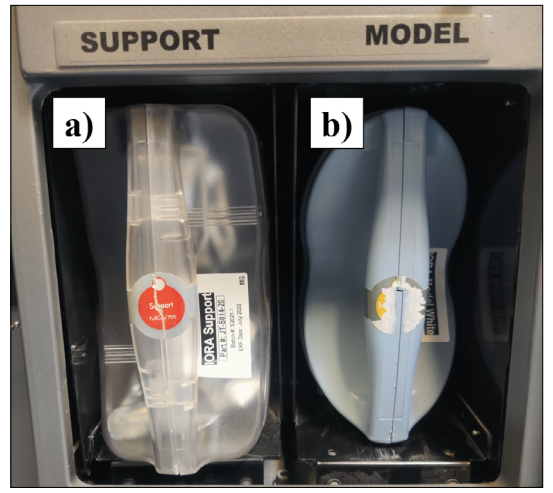


Fig. 3. Materials in the PolyJet printer:
a) support material and b) model material

Table 2. Mechanical properties of IORA Model White RGD835 material [1]

Properties	Value	Standard
Tensile modulus	2000–3000 MPa	ASTM D638
Tensile strength	50–65 MPa	ASTM D638
Elongation at break	13–24%	ASTM D638
Impact strength (IZOD, notched, A 23°C)	20–30 J/mm ²	ASTM D256
Flexural strength	75–110 MPa	ASTM D790
Flexural modulus	2200–3200 MPa	ASTM D790
Deflection temperature (HDT) @ 0,45 MPa	46–51 °C	ASTM D648
Deflection temperature (HDT) @ 1,82 MPa	46–51 °C	ASTM D648
Glass transition temperature (Tg)	52–54 °C	ASTM D4065

2.2. PolyJet 3D printing machine

The test specimens were manufactured using a Stratasys Eden 250 PolyJet 3D printer (Fig. 2). The 3D printer used in this study can process two different types of materials: one for the model and one for the support. The printer's build platform measures 250×250 mm, with a maximum usable printing volume of 200 mm in the Z direction. Its resolution is 600 dpi along the X-axis, 300 dpi along the Y-axis, and 1600 dpi along the Z-axis [7].

2.3. Materials

The printing materials are IORA Support 705 for the support structure and IORA Model White RGD835 for the model material (Fig. 3) [8, 9].

The applied IORA Support 705 material provides excellent stability to ensure that the models maintain their shape and integrity throughout the entire printing process. With the support material, it is easy to create complex and intricate geometries. After printing is completed, the support material can be easily removed using a water jet, ensuring a clean and flawless final result [8].

IORA Model RGD835 materials are versatile and reliable 3D printing materials that belong to the PolyJet photopolymer family and are widely used across various industries. They offer high opacity and tensile strength, making them ideal for producing models that require fine details, such as various casings, fasteners, and prototypes. The high resolution of the PolyJet process ensures that printed parts are extremely precise and have excellent surface quality, which is particularly important for end-use products and precision components. These materials are an ideal choice not only for functional prototypes but also for the production of final products with impeccable aesthetic quality. The key properties of the model material are summarized in Table 2 [9].

2.4. Manufacturing specimens

In high-quality (HS) mode, the layer thickness of the printed test specimens was 16 μm . The specimens were surrounded by support material from all directions. The total printing time was 4 hours and 40 minutes. In high-quality (HQ) mode, the layer thickness was 29 μm , so the software divided the entire print into 1215 layers, with a total manufacturing time of 2 hours and 40 minutes (Fig. 4). The finished test specimens can be easily removed from the build platform using a specialized tool, and the surrounding support material can be washed away with a water jet. The manufactured test specimens are shown in Fig. 5.

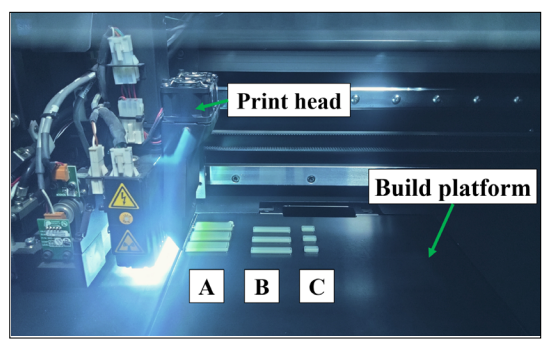


Fig. 4. Objet Eden 250 during the printing process.

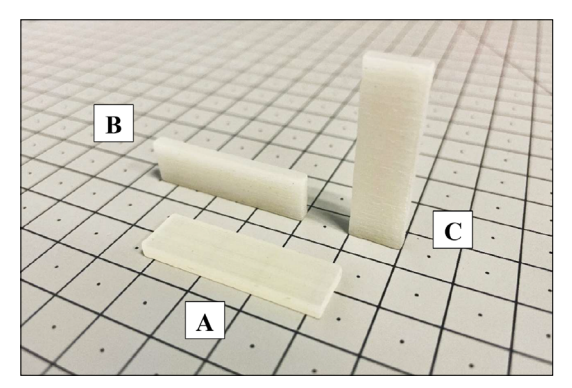


Fig. 5. The finished specimens after cleaning.

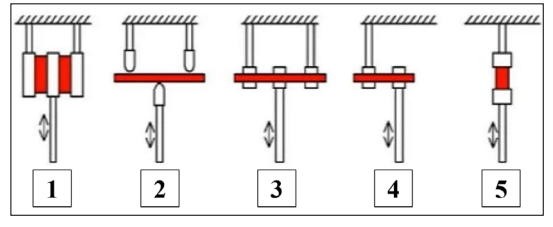


Fig. 6. DMTA measurement modes: 1) shear; 2) threepoint bending; 3) dual cantilever; 4) single cantilever; 5) tension/compression. [10]

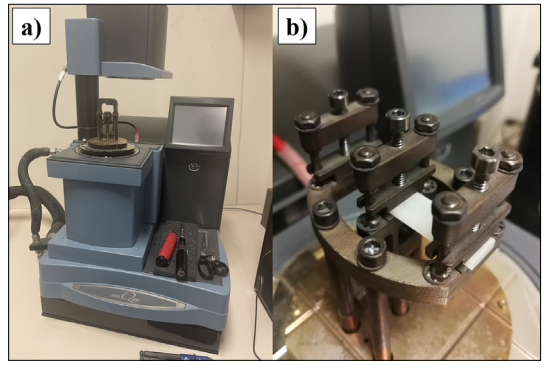


Fig. 7. Measuring equipment: a) TA DMTA Q800 and b) fixed test specimen

After printing, in the case of the PolyJet process, there is no need for post-curing of the test specimens, unlike traditional photopolymerization methods.

3. Testing method

Polymers are often subjected to dynamic loads. Therefore, it is important to understand their behavior under periodic, repetitive loading as well. In DMTA tests, the stress applied to the test specimen and its frequency are kept constant. The temperature is changed in a defined manner (usually at a constant rate over time), and the resulting deformation is measured. Based on these, the mechanical properties of the polymer can be determined. The material testing was conducted on a TA DMTA Q800 device, with a single-sided grip (Fig. 6/4) [1, 10].

The test specimen, with dimensions of 35×10×3 mm, was secured in two screw grips with a torque of approximately 1 Nm (7. ábra). The distance between the two grips was 17.2 mm.

During the DMTA measurement, one end of the test specimen is fixed, while the other is oscillated with a constant amplitude at different frequencies, while the temperature is gradually increased. Before the actual test, preliminary measurements were used to determine the most suitable experimental setup parameters (amplitude, frequency range, temperature range). In our case, the ideal oscillation amplitude was 10 μm . The temperature range was set from 40 to 90°C, with heating occurring in 2°C steps and a 1-minute temperature hold. The test specimen was oscillated at 11 frequencies between 1 and 21 Hz in linear 2 Hz at each temperature.

4. Results

The six different test specimens (orientation A, B, C, as well as HS and HQ settings) were measured individually according to the procedure described above. This study focuses on the glass transition temperature and the loss factor, so these data were primarily presented.

4.1. Frequency dependence of the glass transition temperature

Based on the measurement data, for each frequency, the maximum $Tan(\delta)$ value and the corresponding temperature must be determined. These temperature values were recorded in a table for each test specimen and frequency, and then averaged for the three different orientations of the test specimens. The analysis had to be per-

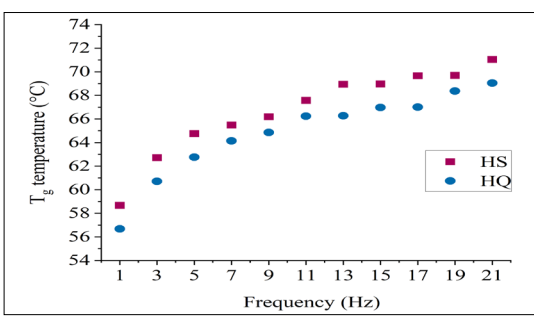


Fig. 8. Frequency dependence of the glass transition temperature.

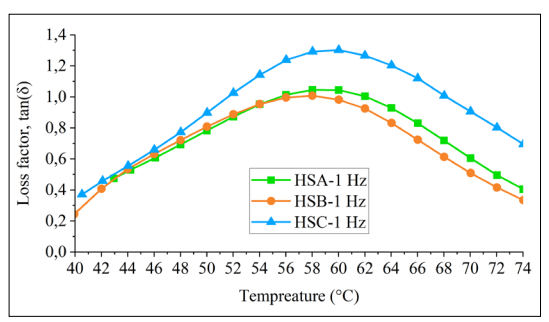


Fig. 9. Loss factor curves as a function of temperature in the high-speed setting.

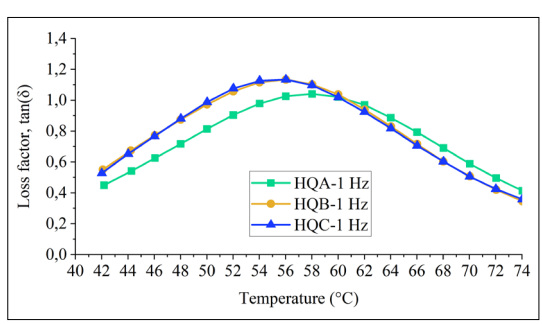


Fig. 10. Loss factor curves as a function of temperature in the high-quality setting.

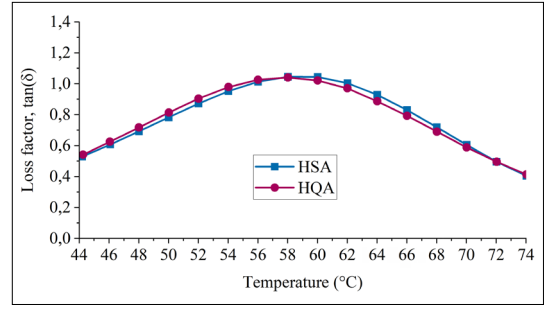


Fig. 11. Loss factor distribution at 1 Hz Frequency: "A" orientation.

formed for both printing settings (HS and HQ). The results are shown in Fig. 8.

The diagram shows that the glass transition temperature (Tg) changes as a function of the excitation frequency. With an increase in frequency, the glass transition temperature of the material increased, which was observed for both printing settings, whether in high speed or high-quality mode. Furthermore, the glass transition temperature of the test specimens produced in high speed mode was approximately 2°C higher than that of the high-quality test specimens.

4.2. Effect of printing orientation on the glass transition temperature

The measurement data can be used to plot the $Tan(\delta)$ curves for each test specimen at a frequency of 1 Hz. As shown in Fig. 9, 10. for both settings, there is a slight but noticeable difference in the $tan(\delta)$ peaks for the test specimens with different orientations, which causes a shift in the glass transition temperatures. The lowest values in the high-speed printing setting are observed in the "A" orientation, while the highest values are found in the "C" orientation test specimens.

4.3. Effect of printing settings on the glass transition temperature

Examining the effect of printing settings on the glass transition temperature, it can be observed that in the "A" orientation, the printing settings have no impact at any frequency (Fig. 11).

However, in the "B" orientation, a difference between the two settings can be observed. The glass transition temperature (T_g) of the high-quality specimen is 2° C lower (Fig. 12).

A similar but slightly larger difference can be observed in the "C" orientation, where the glass transition temperature (Tg) of the specimen printed with the high-quality setting is 4°C higher (Fig. 13).

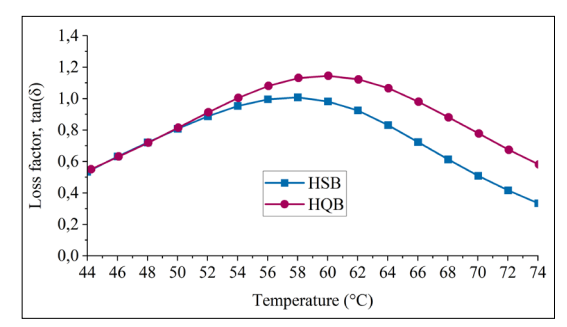


Fig. 12. Loss factor distribution at 1 Hz Frequency: "B" orientation.

This trend in the values can be observed at both low and higher frequencies.

4.4. Effect of printing settings and orientation on the loss factor

From the temperature-loss factor diagrams, it can be observed that the $tan(\delta)$ curves differ not only along the temperature axis but also in their peak values. The loss factor is the ratio of the lost energy to the elastically stored energy. The following diagrams indicate that there are differences in the $tan(\delta)$ peak values depending on both the printing orientations and printing settings (Fig. 14 and 15).

The test specimens printed in the "C" arrangement exhibit the highest $tan(\delta)$ peak values (least elastic), while those printed in the "A" arrangement have the lowest values (most elastic). The frequency has a slight influence on the $tan(\delta)$ peak values. Comparing the printing settings, it can be observed that the high-quality specimens have lower variability in their values. Based on the measurements, it can be concluded that the printing orientation and layer thickness affect the thermomechanical properties of the test specimens. The testing frequency shifts the glass transition temperature towards higher temperatures. The influence of printing orientation has a slight effect on the glass transition temperature, but no clear trend is observed in the results. When comparing the printing settings, it is evident that, except for the "A" arrangement, the high-quality specimens generally exhibit lower glass transition temperatures. Examining the loss factor peak values, the lowest values are found in the "A" arrangements, while the highest values are observed in the "C" test specimens. Based on the obtained results, it can be concluded that the printed products exhibit anisotropic properties.

5. Conclusions

The research examined the mechanical properties of test specimens manufactured by the Poly-Jet 3D printing process, with particular attention given to the effects of printing orientation and layer thickness. The studies found that orientation and layer thickness have a significant impact on the glass transition temperature and the loss factor, which influence the material's mechanical behavior. Higher glass transition temperatures were observed in test specimens printed at higher speeds. This research could contribute to fine-tuning manufacturing parameters, enabling a wider industrial application of PolyJet technology.

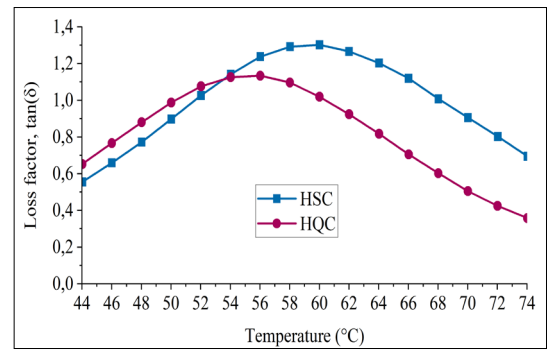


Fig. 13. Loss factor distribution at 1 Hz Frequency: "C" orientation.

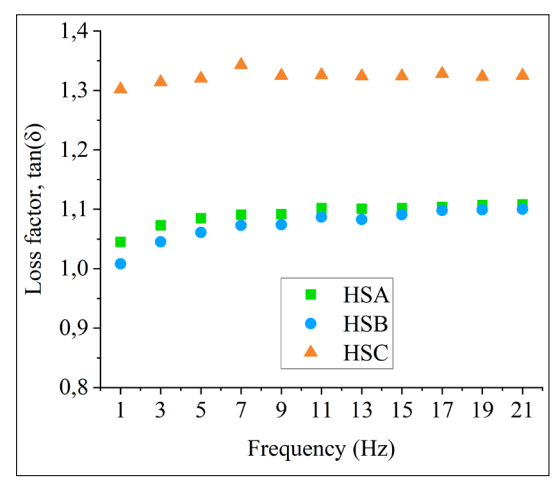


Fig. 14. Maximum values of the loss factor for high-speed specimens.

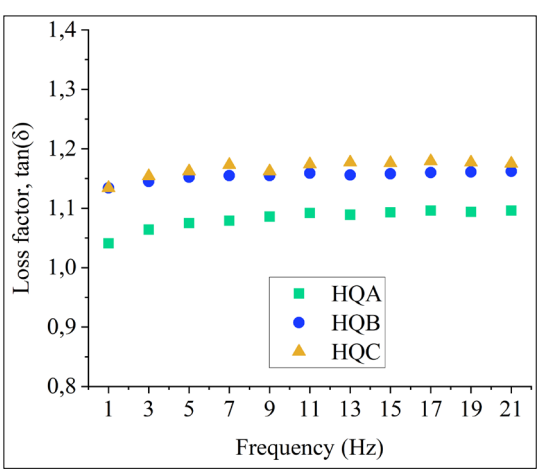


Fig. 15. Maximum values of the loss factor for high-quality specimens.

References

- [1] ISO 14692-1:2018. (accessed on: 2025, 03, 13.) https://www.iso.org/standard/62256.html
- [2] Ficzere Péter: Gyors prototípus numerikus és kísérleti szilárdsági analízise (letöltve: 2025. március 13.)
 - https://repozitorium.omikk.bme.hu/items/ a8911f7c-6529-465d-b544-0f50cd7db8cb
- [3] Sanders, I., Wei, X. & Pei, Z.: Experimental investigation of polyjet 3D printing process: Effects of orientation and layer thickness on thermal glass transition temperature. In: ASME International Mechanical Engineering Congress and Exposition. American Society of Mechanical Engineers, 59377. (2019) V02AT02A064.
 - https://doi.org/10.1115/IMECE2019-11999
- [4] Márk, P. & Sándor, M.: 3D nyomtatási anyagok mechanikai tulajdonságainak meghatározása különböző nyomtatási irányokban. Biomechanica Hungarica, 11/1. (2018)
- [5] Liu, M. L., Reichl, K. K. & Inman, D. J.: Complex modulus variation by manipulation of mechanical test method and print direction. In: Mechanics of Additive and Advanced Manufacturing: Proceedings of the 2017 Annual Conference on Experimental and Applied Mechanics, Springer International Publishing, 9. (2017) 5-11. https://doi.org/10.1007/978-3-319-62834-9_2
- [6] Reichl, K. K. & Inman, D. J.: Dynamic mechanical and thermal analyses of Objet Connex 3D printed materials. Experimental Techniques, 42/1. (2018) 19-25.
 - https://doi.org/10.1007/s40799-017-0223-0

- [7] Falk György: PolyJet a Rapid Prototyping új dimenziója (accessed on: 2025. 03. 13.) http://www.sasovits.hu/cnc/irodalom/3d/PolyJet. pdf
- [8] Stratasys Eden250 3D Printer Support. (accessed on: 2025. 03. 13.) https://support.stratasys.com/en/printers/polyiet-legacy/eden250
- [9] iSQUARED Stratasys Refill IORA Model White 1kg (accessed on: 2025. 03. 13.) https://www.am-material-marketplace.com/ product/iora-model-white-1-kg/
- [10] Polimerek dinamikus mechanikai vizsgálata (DMTA) (accessed on: 2025. 03. 13.) https://docplayer.hu/93271637-3-polimerek-dinamikus-mechanikai-vizsgalata-dmta.html
- [11] Dr. Molnár Kolos: Anyagismereti alapok (letöltve: 2025. március 13.) http://www.pt.bme.hu/futotargyak/97 BMEGEPTBM01_2021oszi/M0T0-Anyagismereti%20alapok%20101.pdf
- [12] Singh, R.: Process capability study of polyjet printing for plastic components. Journal of Mechanical Science and Technology, 25. (2011) 1011-1015.
 - https://doi.org/10.1007/s12206-011-0203-8
- [13] Mueller, J., Shea, K. & Daraio, C.: Mechanical properties of parts fabricated with inkjet 3D printing through efficient experimental design. Materials & Design, 86. (2015) 902-912. https://doi.org/10.1016/j.matdes.2015.07.129



Acta Materialia Transylvanica 8/1. (2025) 8–12.

DOI: Hungarian: https://doi.org/10.33923/amt-2025-01-02

English: https://doi.org/10.33924/amt-2025-01-02



Investigation of the Applicability of Environmentally Friendly Surfactants for Oil Recovery

Ditta Adrienn GERBOVITS, 1 Roland, NAGY 2 Sándor PUSKÁS3

- ¹ University of Pannonia, Veszprém, Hungary, gerbovits.ditta.adrienn@mk.uni-pannon.hu
- ² University of Pannonia, Veszprém, Hungary, nagy.roland.dr@mk.uni-pannon.hu
- ³ MOL Plc, Group Oil Chemical Technologies, Algyő, Hungary, spuskas@mol.hu

Abstract

This study investigates the feasibility of producing surfactants (surface-active agents) from alternative, environmentally friendly raw materials for application in enhanced oil recovery (EOR) processes. The primary objective is to identify and evaluate sustainable feedstocks capable of replacing conventional, widely used surfactant materials that often pose environmental concerns. The paper provides a detailed overview of the analytical and physicochemical methods employed in the characterization of the synthesized surfactants, focusing on key parameters such as surface tension reduction, stability, and emulsification performance. The physicochemical properties of the newly developed surfactants are compared with those of commercially available agents currently used in EOR applications. The ultimate goal of this research is to support the development of sustainable and eco-conscious alternatives that maintain or improve oil recovery efficiency while minimizing environmental impact.

Keywords: enhanced oil recovery, sustainability, environmentally friendly, surfactant.

1. Introduction

In the context of global energy demands, a key ambition is to extract oil from oil fields and reservoirs with maximum efficiency. When the residual oil trapped in the reservoir rock cannot be recovered by conventional recovery methods, an Enhanced Oil Recovery (EOR) process is employed. [1]. This process involves the use of an additive that changes the chemical and physico-chemical properties of the oil in the porous rock (reservoirs), making it more mobile and easier to bring to the surface [2]. The fundamental principle underpinning the method is that the auxiliary substances employed act on the forces that hold the oil in the pores of the reservoir rock, thereby preventing it from flowing out [3]. EOR technologies can utilise several types of auxiliary substances, which can be thermal, gas injection, chemical or other auxiliary substances. The type of extraction process employed is contingent on the geological properties of the reservoir, the physical and chemical characteristics of the oil and the composition of the reservoir water [4, 5, 6]. The methods employed are delineated in Fig. 1 [7]:

The remainder of this study focuses on the analysis of surfactants employed in chemical enhanced oil recovery (cEOR) processes. As illustrated in Fig. 1., the auxiliaries of the chemical process encompass polymers, surfactants, alkalis, and foaming agents [8]. The concurrent utilisation of these auxiliaries can elicit synergistic effects. The present study investigates the surfactants utilised in petroleum extraction processes, with a view to replacing the conventional surfactant feedstocks with eco-friendly vegetable oil alternatives. The syntheses undertaken in this study focus on the preparation and testing of geminitype surfactants, which represent a distinct group of surfactants. Gemini surfactants are compounds that possess dimeric structures. In contradistinction to simple surfactants, gemini surfactants possess two long hydrophobic hydrocarbon chains and two hydrophilic headgroups, which are connected by a spacer. Their schematic structure is shown in Fig. 2.

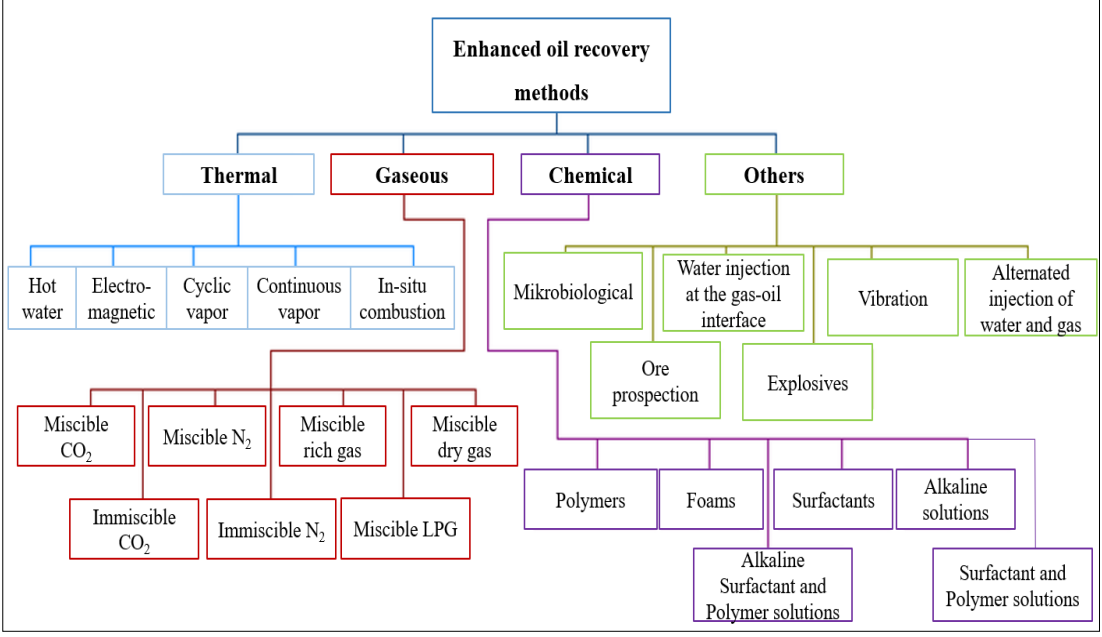


Fig. 1. Additives used in enhanced oil recovery processes (LPG-liquefied petroleum gas) [7]

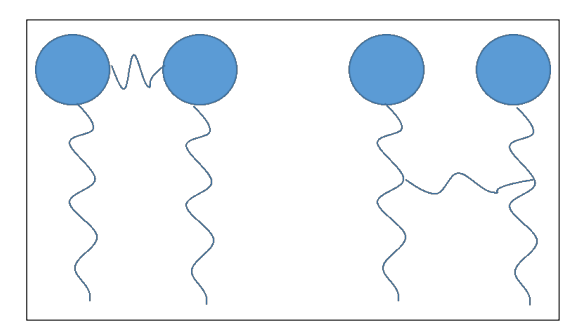


Fig. 2. Schematic structure of gemini surfactants.

2. Raw materials

The following paper presents the results of an experimental study into the physical and chemical properties of the plant-based surfactant KO-MAD-710, developed, produced and marketed by MOL Plc., the coconut oil-based surfactant Empilan 2502, the oleic acid-based surfactant SPAN80 marketed by SigmaAldrich, and two proprietary sunflower-based experimental gemini surfactants (experimental surfactants ZMG-1 and ZMG-3).

The experimental work, which analyzes the physical and chemical properties and impact assessment of commercially available surfactants,

is shown in **Table 1** were analysed. All the surfactants investigated belong to the non-ionic group.

Our own experimental surfactants are gemini-type non-ionic surfactants based on vegetable oil. The synthesis of the experimental surfactants presented in the following chapters is broadly similar, the only difference being the number of carbon atoms in the spacers used, but in both cases the compound used was dibromoalkane.

The first step in preparing the experimental surfactants was to make a glycerol ester intermediate by transesterification from vegetable oil and glycerol. Then, the glycerol ester intermediate was reacted with dibromoalkane in an alkaline cyclic medium using a phase transfer catalyst. The reactions were carried out at 100-250 °C and ambient pressure. The product was dried with anhydrous sodium sulphate [9].

3. Methodology

The physical and chemical properties of the surfactants and the impact studies were evaluated and carried out using the following methods.

3.1. Density and dynamic viscosity

Density and dynamic viscosity were measured at 40 °C using an SVM 3000 Stabinger Viscometer.

Brand of surfactant	KOMAD- 710	Empilan 2502	SPAN80
Raw material	Rapeseed oil	Coconut oil	Sorbitol
Distributor	MOL Nyrt.	Huntsman	Sigma-Aldrich

Table 1. Commercially available surfactants and their environmentally friendly base materials

3.2. The pH value

The pH was measured in a 5 g/l distilled aqueous solution of the surfactants using a SevenCompact Duo from Mettler Toledo.

3.3. Solubility

The solubility of the surfactants in water was also tested in a 5 g/l distilled aqueous solution by visual inspection and transmittance measurement. Transmittance was measured using an Avantes AvaSpec-DUAL spectrophotometer.

3.4. Pour point

The pour point was measured with a Koehler automatic pour point and freezing point meter.

3.5. Water number

The test is used to determine the hydrophilic-lipophilic nature of surfactant compounds, thus providing information on the emulsifying effect of surfactants and their salt tolerance. The water number was determined by titration. The measurement was carried out by dissolving 1 g of surfactant in 30 cm³ of a 4:96 mixture of cyclohexane-acetone and titrating the mixture with distilled water until turbidity was reached.

3.6. Oil displacement test

The oil displacement test is performed by thin film chromatography. To prepare for the test, we dipped a clean, dry glass plate into a chloroform suspension of the powdered rock material from Algyő. This caused a thin layer of powdered rock to form on the glass plate after it dried. We applied a droplet of Algyő 892 petroleum about 2 cm from the bottom of the glass plate. We made a solution of the surfactants in Algyő filtered brine water that had 5 g/l of it. Then we measured out 15 cm³ of the prepared solution and put it into test tubes. We put the prepared glass plates inside the test tubes and sealed the test tubes. We then placed the samples in a drying oven at 60 °C for 3 hours. At the end of the test, the distance between the oil spot and the edge of the plate was measured. The result is given in millimetres.

3.7. Emulsifying (solubilising) effect test

The emulsifying effect was tested using an ADEM automatic emulsifier. During the test, 40 cm³ of a 5 g/l concentration of a surfactant solution prepared with filtered brine water from Algyő was measured into the measuring cylinders of the device, and 40-40 cm³ of Algyő 892 oil was added to each sample. The samples were stirred at 1500 rpm (revolutions per minute) for 2 minutes. After half an hour, the resulting emulsion (mixture) was analysed.

3.8. Interfacial tension (IFT) test

The interfacial tension (the force that keeps water and oil apart) was measured using a special tool called a Krüss SDT Spinning Drop Tensiometer. This tool has a thin glass tube (called a capillary) that is spun around a central axis. The radius of the oil droplet in the capillary is measured from the axis of rotation. This allows us to calculate the interfacial tension between the surfactant solution in the capillary and the oil droplet. In this study, we also used Algyő 892 oil and a solution of the surfactants in 5 g/l Algyő filtered brine water.

4. Results

The values obtained from analysing the surfactants physically and chemically are shown below Table 2 shows the physical and chemical properties of the surfactants that were tested. Table 3 shows the results of the impact tests.

5. Conclusions

The aim of this experimental work was to produce surfactants from renewable raw materials that are less harmful to the environment and can be used in petroleum extraction, to replace surfactants that are already commercially available.

The results of the measurements show that the experimental surfactant ZMG-1 has the highest oil displacement efficiency measured by thin-layer chromatography, the highest emulsification efficiency compared to all commercially available surfactants, and the interfacial tension test is in

Properties/Sign of surfactant	KOMAD- 710	Empilan 2502	SPAN80	ZMG-1	ZMG-3
Density (g/cm ³) 40 °C	0.9701	0.9800	0.9860	1.2201	1.2223
Dynamic viscosity (mPa·s) 40 °C	148.8	450	1285	1.6570	1.5947
pH-value	11.21	9.74	Not measurab- le	12.83	11.83
Pour point (°C)	-25	9	1	-15	-16
Solubility	Soluble	Partially soluble	Non-soluble	Soluble	Soluble
Transmittancy (%)	34	51	69	23	28
Water number (cm³)	10.3	13.5	4.30	13.0	11.65

Table 2. Physical and chemical properties of the tested surfactants

Table 3. Results of the impact assessments of the tested surfactants

Properties/Sign of surfactant	KOMAD- 710	Empilan 2502	SPAN80	ZMG-1	ZMG-3
Oil displacement test, (mm)	21	12	10	26	20
Emulsifying (solubilising) effect test, (V/V%)	30	22	23	41	63
IFT (mN/m)	6.18	8.67	10.2	7.14	5.3

the order of magnitude of the other surfactants.

The oil displacement test of the experimental surfactant ZMG-3 showed that the oil droplet "ran" almost twice as far as Empilan 2502 and SPAN80, and performed similarly to KOMAD-710. In the emulsifying effect test, the experimental surfactant ZMG-3 showed the highest result. The value of interfacial tension is also more favourable compared to the interfacial tension measured for the other tested surfactants.

Overall, the preliminary efficacy assessment of the surfactants suggests that the experimental surfactants have similar or even superior efficacy to the existing surfactants on the market.

References

- [1] Gbadamosi, A. O., Junin, R., Manan, M. A. et al.: An overview of chemical enhanced oil recovery: recent advances and prospects. International Nano Letters, 9. (2019) 171–202. https://doi.org/10.1007/s40089-019-0272-8
- [2] Wan-Li K., Bo-Bo Z., Issakhov M., Gabdullin M.: Advances in enhanced oil recovery technologies for low permeability reservoirs. Petroleum Science, 19/4. (2022) https://doi.org/10.1016/j.petsci.2022.06.010.

- [3] Barman B. N., Cebolla V. L., Mehrotra A. K., Mansfield C. T.: *Analytical Chemistry. Petroleum and Coal*, 73. (2001) 2791–2804.
- [4] Agi A., Junin R., Syamsul M. F., Chong A. S., Gbadamosi A.: *Intermittent and short duration ultrasound in a simulated porous medium*. Petroleum, 5/1. (2019) 42–51. https://doi.org/10.1016/j.petlm.2018.03.012.
- [5] Gbadamosi A., Patil S.; Kamal, M. S., Adewunmi A. A., Yusuff A. S., Agi A., Oseh J.: Application of Polymers for Chemical Enhanced Oil Recovery. A Review. Polymers 14. (2022) 1433. https://doi.org/10.3390/polym14071433
- [6] Tavakkoli O., Kamyab H., Shariati M., Mohamed A. M., Junin R.: Effect of nanoparticles on the performance of polymer/surfactant flooding for enhanced oil recovery. A review. Fuel, 312. (2022) https://doi.org/10.1016/j.fuel.2021.122867.
- [7] Gurgel A., Moura M. C., Castro T. N. D., Barros Neto E. L., Dantas Neto A. A.: A review on chemical flooding methods applied in enhanced oil recovery. Brazilian Journal of Petroleum and Gas, (2008), 2.
- [8] Samanta A., Bera A., Ojha K. et al.: Comparative studies on enhanced oil recovery by alkali-surfactant and polymer flooding. Journal of Petroleum Exploration and Production Technology, 2. (2012)

67–74. https://doi.org/10.1007/s13202-012-0021-2

[9] Pal N., Kumar N., Verma A., Ojha K., Mandal A.: Performance Evaluation of Novel Sunflower Oilbased Gemini Surfactant(s) with different Spacer Lengths. Application in Enhanced Oil Recovery, Energy&Fuels, 32. (2018) 11344–11361. https://doi.org/10.1021/acs.energyfuels.8b02744



Acta Materialia Transylvanica 8/1. (2025) 13–16. DOI: magyar: https://doi.org/10.33923/amt-2025-01-03 angol: https://doi.org/10.33924/amt-2025-01-03



Production of Fibre Mats from Recycled PET Bottles

József KÁNTOR,¹ Attila Levente GERGELY²

- ¹ Sapientia Hungarian University of Transylvania, Faculty of Târgu Mureș, Department of Mechanical Engineering, Târgu Mureș, Romania, kantorjozsef@ms.sapientia.ro
- ² Sapientia Hungarian University of Transylvania, Faculty of Târgu Mureș, Department of Mechanical Engineering, Târgu Mureș, Romania, agergely@ms.sapientia.ro

Abstract

The excessive use of polymer materials in the packaging industry and improper waste management greatly contribute to environmental pollution. The recycling of this plastic waste is key to improving sustainability. In this paper the production of non-woven fibre mats from PET bottles was studied, which can be used in air filtration. The fibres were generated using centrifugal spinning. The potential to substitute the common solvents of PET with less harmful ones was also investigated.

Keywords: PET, centrifugal spinning, microfibre, recycling.

1. Intorduction

Polyethylene terephthalate (PET) is the sixth most produced polymer with ~56 million tons being synthesized and manufactured into goods each year. Roughly 40% of this amount is used in the packaging industry (foils, bottles, boxes), and another 45% in the textile industry. Considering the nature of its uses, the amount of PET waste produced yearly is also high [1].

There are various ways to recycle PET, one of them is the production of nano- and microfibres. The most common technique to produce non-woven nanofibre mats is electrospinning. Other possible methods are melt blowing and centrifugal spinning. One of the primary aims during fibre production is to minimize the fibre size [2]. Melt spinning does not require the use of solvents at all, however the equipment is more complex, and the in the case of PET the average fibre diameter of the produced fibres is around an order of magnitude larger [3].

During centrifugal spinning a chamber that contains the polymer solution is rotated at 4000-15 000 1/min. Due to the centrifugal force, the polymer solution ejects from the chamber through radial capillaries, creating liquid jets. As the jets travel through the air the solvent evaporates, and the dry fibres deposit on the collector. Despite a simple setup, centrifugal spinning has a high pro-

duction rate even under laboratory conditions. In addition, the electrical conductivity of the solution does not influence the process, and there is no need for a high voltage source, as in the case of electrospinning [2].

Vo et al. . successfully produced PET fibres with centrifugal spinning from PET solutions in a mixture of trifuloroacetic acid (TFA) and dichloromethane (DCM) in a 70/30 mass ratio. The experimental setup involved various capillary diameters (160-340 μ m), rotational speeds (6000-15 000 1/min), and solution concentrations (5-13% PET). The average diameter of the fibres that did not contain beads were between 0.66±0.27 and 4.26±2.32 μ m, depending on the process parameter [4].

Since PET is a semi-crystalline polymer, it doesn't readily dissolve in most organic solvents. In general PET solutions are prepared with acidic solvents, most often with TFA. In some published studies the mixture of TFA and DCM is featured in 70/30 and 50/50 mass ratios [4, 5]. The problem with fluorinated acids is that they are toxic and persist for a long time in the environment. The half-life of TFA in aquatic ecosystems is on the scale of around a hundred years [6]. CTherefore, it is crucial to look for alternatives.

The solubility of polymers can be studied with the help of the Hansen solubility parameters (HSP). According to the model, the solubility of every chemical compound is determined by 3 interaction parameters, that represent the potency of dispersion (δD), polar (δP) and hydrogen bonding (δH) intermolecular forces. The closer the HSPs of the polymer are to that of the solvent, the better the solubility [7].

2. Experimental

2.1. Materials

Polyethylene terephthalate (PET) was acquired from a mineral water bottle. Trifuoroacetic acid (TFA, Sigma Aldrich, 99%), phenol (Thermo Scientific, 99%), dichloromethane (DCM, VWR Chemicals, 99.8%), dimethyl formamide (DMF, VWR Chemicals, 98%), and toluene (VWR Chemicals, 99.9%) were used as received.

2.2. Polymer solution preparation

15% PET solution was prepared with 15/85 mass ratio TFA/DCM solvent mixture, and 10, 12.7, 15, and 20% solutions with 30/70 TFA/DCM mixture in 20 ml vials. The contents of the vials were stirred with a magnetic stirrer for 24 hours at room temperature. For solubility studies 10% PET was added to 50/50 mixture of phenol and DCM, as well as 55/45 mixture of toluene and DMF.

2.3. Centrifugal spinning

Centrifugal spinning was performed with a custom-built setup [8]. A chamber (spinneret) with two radial capillaries (25G needles) was rotated by an electric motor at 4000-8000 1/min. The polymer solution was fed into the spinneret through a teflon tube at 60 mL/h with the help of a syringe pump. Fibres were collected on 8 radially positioned steel rods with a needle-collector distance of 100 mm. All experiments were performed at 22°C and 40% relative humidity.

2.4. Scanning Electron Microscopy (SEM)

SEM was performed using a JEOL JSM-5200 scanning electron microscope at 15 kV accelerating voltage on uncoated samples. The PET fibre diameters were measured with the open-source ImageJ software, and 50 measurements were taken on each image.

2.5. Solubility calculations

The Hansen solubility parameters (HSP) of PET and the solvents can be found in the literature [7].

The HSP distance (R_a) can be interpreted as the radius of a sphere, that is calculated from the difference of the position vectors of the polymer and

the solvent in the HSP space, as follows:

$$R_a = \sqrt{4 \cdot (\delta D_2 - \delta D_1)^2 + (\delta P_2 - \delta P_1)^2 + (\delta H_2 - \delta H_1)^2}$$
(1)

where a δD , δP and δH denote the dispersion, polar, and hydrogen bond interactions, while the lower indices 1 and 2 refer to the polymer and the solvent, respectively. The dispersion term is multiplied by 4, based on empirical data [7].

3. Results and Discussion

The 15% PET in 15/85 TFA/DCM did not dissolve even after 24 hours of constant stirring. For this reason, fibres were not produced at this concentration. In order to increase the solubility of PET the amount of TFA was increased, resulting in a 30/70 TFA/DCM solvent ratio. 10, 12.7, and 15% PET were fully dissolved in the solvent mixture, however at 20% only partial dissolution was achieved.

Centrifugal spinning was performed with the 10, 12.7, and 15% solutions, each time at 3 different rotational speeds. Out of the nine attempts only the spinning of the 10% solution at 6000 and 8000 1/min and the 12.7% solution at 4000 and 6000 1/min resulted in fibre generation. The 10% solution at 4000 1/min produced mostly droplets, while the 12.7% solution at 8000 1/min, and the 15% solution at all rotational speeds produced only short fibre segments that could not be captured by the collector rods.

The SEM images are shown in Fig. 1. The images show that the generated fibres contained beads at all conditions. According to the literature beading can be reduced with the increase of the polymer concentration, which is due to the increased solution viscosity, and thus the higher viscoelastic tensile forces that oppose the surface tension [9]. In our case increasing the PET concentration from 10 to 12.7% did not result in a lower bead density, and at 15% the formation of continuous fibres ceased.

The fibre diameters were measured from the SEM images, and the results can be seen in **Table 1**. The results show that there was a slight increase in average fibre diameter and standard deviation as the rotational speed increased. The most noticeable increase in fibre diameter, approximately 28%, was observed in the case of the 12.7% solution. Based on the SEM data the most favorable conditions in regards of fibre size were the 10% solution concentration and 6000 1/min rotational speed, resulting in both the lowest average size and lowest deviation. The fiber mats

showed a slight orientation perpendicular to the axis of the spinneret.

The PET solution preparation experiments showed that the TFA and DCM solvent ratio greatly affected the solubility of PET. In the majority of the published literature PET solutions are prepared either with a 70/30 or 50/50 mass ratio of TFA and DCM. In this study complete dissolution and fibre formation was achieved with a 30/70 TFA/DCM solvent mixture, which is a significant reduction in acid usage. On the other hand, the average diameter of fibres produced under similar conditions, but from a 70/30 TFA/DCM mixture was smaller (0.66±0.27 μ m) [4].

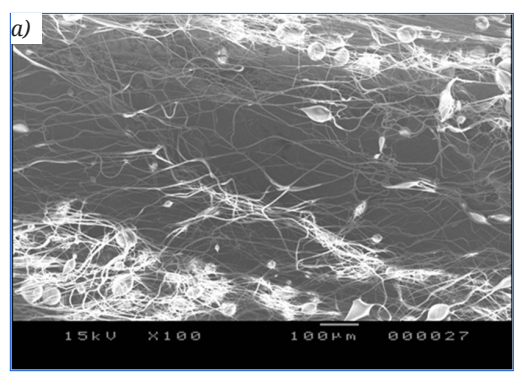
In order to study the dissolution phenomenon of PET in more detail, the Hansen solubility parameters can be used. **Fig. 2** shows the solubility parameters of PET and some other chemicals that may be given consideration as a potential solvent. For reference, water was also added to the plot. It can be seen, that DCM is located close to PET (R_a = 2.06), which would indicate that it is a good solvent, however our experiments showed that pure DCM does not in fact dissolve PET. In contrast, TFA is further away on the chart (R_a = 6.71),

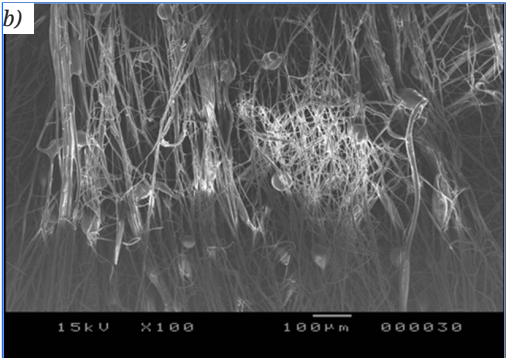
Table 1. Average fibre diameters and standard deviations

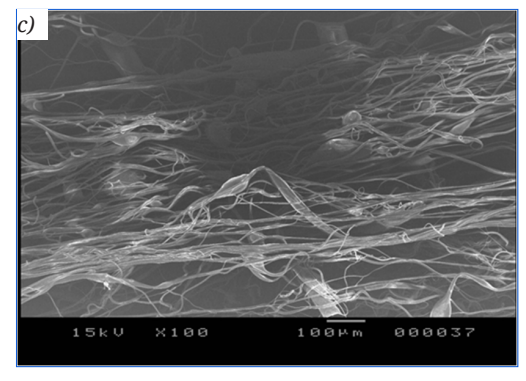
Concentration	Rotational speed (1/min)	Fibre diameter (µm)
100/	6000	1.72±0.63
10%	8000	1.94±0.98
40.70/	4000	1.89±0.84
12.7%	6000	2.42±1.37

and yet it dissolves PET. Our hypothesis is that this is due to the semi-crystalline nature of PET, and the key to the dissolution is the acidity of the TFA, which is not accounted for in the Hansen solubility model.

Experiments with other solvent mixtures resulted in the PET dissolving in 50/50 mixture of DCM and phenol (R_a =2.88), which is a weak acid. It should be noted that phenol-based solutions are unfit for fibre production, as phenol is a crystalline solid at room temperature, and it does not evaporate during fibre generation. PET did not dissolve in 55/45 DMF/toluene (not acidic), albeit the HSP distance was particularly low in this case (R_a =1.57). As a continuation of the project, solu-







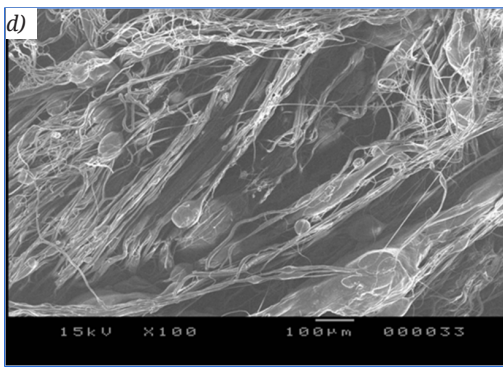


Fig. 1. SEM micrographs of the PET fibre mats at 100× magnification. a) 10%, 6000 1/min, b) 10%, 8000 1/min, c) 12.7%, 4000 1/min, d) 12.7%, 6000 1/min.

bility experiments with amorphous PET can be attempted, in which case the acidity of the solvents might not play a significant role.

4. Conclusions

PET-based non-woven fibre mats were successfully created with centrifugal spinning from recycled water bottles. 10% PET concentration, 30/70 TFA/DCM solvent ratio, and 6000 1/min rotational speed proved to be the optimal conditions, resulting in fibres with 1.72±0.63 μm in diameter. Under all conditions beads were present in the fiber mat, so further optimization of the production parameters is necessary. In addition, we studied the solubility of PET with the Hansen solubility model. According to the model, multiple substances should act as a solvent, however the results indicate that an acidic medium is required for the dissolution of semi-crystalline PET.

Acknowledgements

Attila Gergely wishes to thank the Transylvanian Museum Society for the financial support (contract no. 407.8.1 /2023)...

References

- [1] Soong Y.-H. V., Sobkowicz M. J., Xie D.: Recent Advances in Biological Recycling of Polyethylene Terephthalate (PET) Plastic Wastes. Bioengineering, 9. (2022) 98–124.
- [2] Rogalski J. J., Bastiaansen C. W. M., Peijs T.: Rotary Jet Spinning Review a Potential High Yield Future for Polymer Nanofibers. Nanocomposites, 3. (2017) 97–121.
- [3] Qin Y., Qu M., Kaschta J., Schubert, D. W.: Comparing Recycled and Virgin Poly (Ethylene Terephthalate) Melt-Spun Fibres. Polymer Testing, 72. (2018) 364–371.
- [4] Vo P., Doan H., Kinashi K., Sakai W., Tsutsumi N., Huynh D.: *Centrifugally Spun Recycled PET: Processing and Characterization*. Polymers, 10. (2018) 680–693.

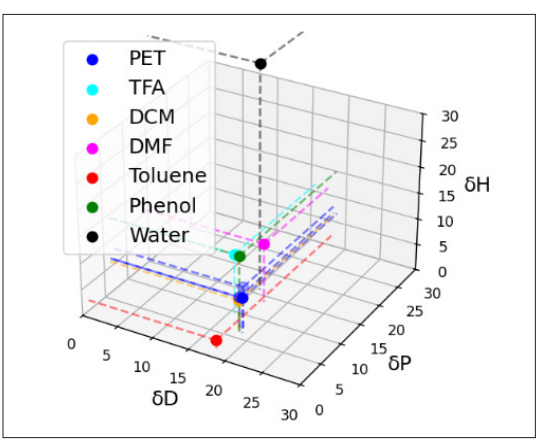


Fig. 2. Hansen solubility parameters of PET and various solvents. The labels on the axes represent the δD – dispersion, δP – polar, δH – hydrogen bond components.

- [5] Jafari S., Hosseini Salekdeh S. S., Solouk A., Yousefzadeh M.: Electrospun Polyethylene Terephthalate (PET) Nanofibrous Conduit for Biomedical Application. Polymers for Advanced Techs, 31. (2020) 284–296.
- [6] Ellis D. A., Hanson M. L., Sibley P. K., Shahid T., Fineberg N. A., Solomon K. R., Muir D. C. G., Mabury S. A.: The Fate and Persistence of Trifluoroacetic and Chloroacetic Acids in Pond Waters. Chemosphere, 42. (2001) 309–318.
- [7] Hansen C. M.: Hansen Solubility Parameters: A User's Handbook. 2nd edition. CRC Press, Boca Raton, 2007.
- [8] Fábián H., Gergely A.: Design of a High Performance Fiber-Producing Machine. Acta Materialia Transylvanica, 5. (2022) 62–65. https://doi.org/10.33924/amt-2022-02-03
- [9] Reneker D. H., Yarin A. L., Fong H., Koombhongse S.: Bending Instability of Electrically Charged Liquid Jets of Polymer Solutions in Electrospinning. Journal of Applied Physics, 87. (2000) 4531–4547.



Acta Materialia Transylvanica 8/1. (2025) 17–22. DOI: magyar: https://doi.org/10.33923/amt-2025-01-04 angol: https://doi.org/10.33924/amt-2025-01-04



Improving the Properties of UNIMAX Tool Steel by Surface Coating

Olivér Gábor KERTÉSZ,1 László TÓTH 2

- ¹ Bánki Donát Faculty of Mechanical and Safety Engineering, Óbuda University, Budapest, Hungary, k.oliver0917@gmail.com
- ² Bánki Donát Faculty of Mechanical and Safety Engineering, Óbuda University, Budapest, Hungary, toth.laszlo@bgk.uni-obuda.hu

Abstract

The aim of this study was to determine the extent to which surface coating can improve the service life and mechanical properties of tools made from UNIMAX steel. Two specimens with identical composition and heat treatment were used, one of which was coated with a CrAIN-based BALINIT FORMERA layer. Microhardness measurements, wear tests, and microscopic analyses were carried out during the investigation. The results clearly demonstrated that the coating significantly increases the tool's lifetime and enhances its mechanical properties.

Keywords: tool steel, tool service life, surface coating, material testing.

1. Introduction

In our previous research, we focused on extending the service life of a pressure die-casting tool. During these studies, we were able to determine an optimal material grade and its corresponding heat treatment. As further opportunities to increase tool life, we identified the investigation of coating technologies [1].

The UNIMAX tool steel, produced by Uddeholm, can be applied in a wide range of tooling, for example:

- plastic forming tools
- hot forming tools
- pressure die-casting tools.

The combination of short cycle times and long service life contributes to cost-effective production. Tools manufactured from this material exhibit high hardness and wear resistance while maintaining toughness [2]. The excellent properties of UNIMAX steel are due to its electroslag remelting process, which results in minimized sulfur content, segregation, and nonmetallic inclusions [3]. The steel is highly pure, with enhanced homogeneity and good hot toughness.

Due to controlled solidification, a fine-grained structure and smaller carbide particles are obtained. This steel is alloyed with chromium, molybdenum, and vanadium, providing excellent hot toughness, temper resistance, and surface treatability (Table 1).

Table 1. Chemical composition of UNIMAX tool steel

c	Si	Mn	Cr	Mo	V
0.50	0.20	0.50	5.00	2.30	0.50

After heat treatment, it exhibits good dimensional stability and polishability. These favorable properties can be further enhanced through the appropriate heat-treatment technologies, including:

- optimal hardening temperature
- cryogenic treatment
- carefully selected tempering temperatures
- multiple tempering cycles.

It has been proven that cryogenic treatment can significantly increase the lifetime of UNIMAX steel die-casting tools by minimizing the amount of retained austenite [4].

In our study, we investigated how tool life could be further increased and how even more favorable properties could be achieved through the application of suitable surface coating technologies [5].

Surface treatments improve wear resistance, surface hardness, and corrosion resistance. The

purpose of coating is to create a thin, high-hardness surface layer with low friction, minimal adhesion, high wear resistance, and corrosion resistance [6].

One of the most widely used methods is PVD coating. In this process, the coating material is evaporated in a vacuum and deposited onto the finished tool surface. The coating forms an approximately 1-micron-thick layer that adheres firmly to the tool. The process is generally carried out below 600 °C, which does not affect the base hardness of the tool.

The coating we used is BALINIT, produced by Oerlikon Balzers, a leading player in the coating industry. BALINIT coatings are multifunctional, have unique properties, and enhance the long-term cost-effectiveness and productivity of manufacturing processes. They provide high surface hardness, protecting the tool against wear and erosion. The coating consists of a ceramic material with a low friction coefficient, preventing adhesive and abrasive wear, molten metal sticking, and improving demolding [7]. It also ensures excellent thermal and chemical stability, resulting in no oxidation and reduced contamination of the tool by the melt. Furthermore, it provides protection against heat checking [8].

Thanks to these properties, BALINIT coatings reduce tooling costs, increase service life, and lower production costs, downtime, losses, and maintenance expenses [9].

The specific coating we selected is BALINIT FORMERA ADVANCED. This coating focuses on solving heat checking, preventing adhesion, and providing corrosion protection. As a result, the tool does not require cleaning or maintenance after casting, thereby reducing downtime.

2. Materials, Equipment, and Technologies

2.1. Material Selection

The test specimens examined in our study were made from the base material of a hot-forming die, designed for the production of automotive aluminum components. For hot-forming tools, essential properties include wear resistance, resistance to thermal fatigue, high hardness, as well as good hot toughness [10]. The Uddeholm UNIMAX tool steel we selected is a premium-quality material that perfectly meets these requirements.

Its high carbon content increases hardness, while chromium alloying is responsible for the formation of complex carbides. Molybdenum, in addition to contributing to carbide formation,

also enhances hot toughness and temper resistance. Vanadium is responsible for grain refinement and ensuring good wear resistance [11].

2.2. Equipment and Devices

2.2.1. Heat Treatment Furnace

The heat treatments were carried out at Titán 94 Ltd. in Lőrinci, using a Schmetz-type electric vacuum furnace. In this furnace, tool heating is performed under vacuum, cooling is achieved by nitrogen as protective gas, while cryogenic treatment is carried out by spraying liquid nitrogen into the chamber, reaching –150 °C.

In Fig. 1 the furnace interior shows the graphite heating rods on both sides, the flexible thermocouple in the middle, as well as the fan and injection nozzles located at the back of the furnace through which nitrogen is introduced. The 8 test specimens and the installed Ni-NiCr thermocouples serve for process control and monitoring.

Fig. 2 illustrates the furnace setup. The liquid nitrogen tank is visible, nitrogen inlet valves are highlighted in green, while the blue color represents the water cooling of the double-walled furnace. On the left side, the two vacuum pumps belonging to the furnace can be seen.

2.2.2. Coating Furnace

The coating furnace is an INNOVA-type device (Fig. 3), with an inner chamber size of 700×1200 mm, into which tools can be mounted on a carousel element. Prior to coating, the tools undergo both chemical and mechanical cleaning. After loading the workpiece into the chamber, it is evacuated to 10^{-6} mbar [12]. The surface treatment process continues with evaporation of the coating source, which generates a plasma cloud inside the furnace chamber. Nitrogen gas is introduced into this plasma. The atoms and ions evaporated from the source disks condense onto the workpiece surface through adhesion. This process continues until the desired coating thickness is achieved.

2.2.3. Preparation for Measurements

For the examinations, test specimens had to be cut out first, which was carried out using the Servocut 302 abrasive cutting machine, shown in Fig. 4.

After cutting, sample preparation followed, consisting of hot mounting, grinding, polishing, and etching. Grinding and polishing were performed with a Forcipol 102 grinding-polishing machine (Fig. 5) while etching was carried out with 4% Nital.



Fig. 1. Interior of the furnace.

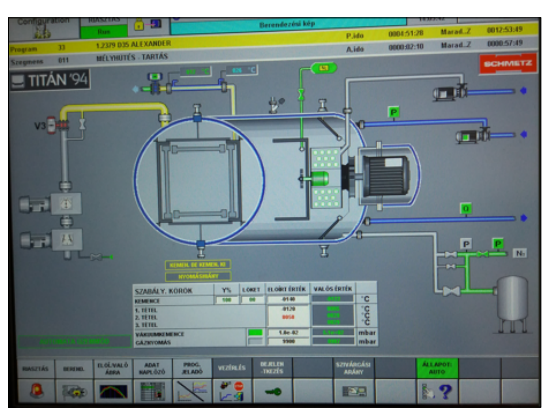


Fig. 2. Furnace control monitor.



Fig. 5. Grinding-polishing machine.



Fig. 3. INNOVA coating equipment.



Fig. 4. Servocut cutting machine.

2.2.4. Coating Thickness Measurement

The aim of the measurement was to determine the thickness of the deposited coating. Ultrasonic pulses were directed to the surface, which were reflected from the interface between the coating and the tool steel. Using the propagation speed of the reflected wave and the elapsed time, the coating thickness was calculated with the following equationl:

$$D = (v \times t) / 2,$$
 ahol (1)

D: coating thickness. v: propagation speed.

t: time.

2.2.5. Microhardness Testing

Microhardness measurements were performed using a KB 30S video hardness tester, illustrated in Fig. 6.



Fig. 6. Microhardness tester.

2.3. Heat Treatment

2.3.1. Stress-Relief Annealing

The first essential step in heat treatment was stress-relief annealing. The tool was slowly heated up to 650 °C in a nitrogen protective atmosphere, held at this temperature for two hours, and then slowly cooled to room temperature. This step is necessary because internal stresses accumulate during tool manufacturing, which promote crack initiation or potential fractures [13]. Annealing reduces this risk, thereby increasing the service life of the tool [14].

2.3.2. Hardening

The next heat treatment was hardening, which can be divided into two stages. The first stage was austenitization: the material was heated stepwise up to the hardening temperature and held until homogeneous austenite was formed. The second stage involved cooling in nitrogen gas at a rate faster than the critical cooling speed, down to room temperature, with the goal of producing a martensitic microstructure.

Stepwise heating was applied to equalize temperature differences between the surface and the core of the material and to prevent stresses caused by phase transformations. The hardening of UNIMAX was carried out at 1050 °C.

2.3.3. Cryogenic Treatment

For further improvement of tool life, cryogenic treatment was applied to the tool after cooling to room temperature [14]. Following hardening, the

test specimens were cooled further to –150 °C using sprayed liquid nitrogen. Cryogenic treatment improves microstructural homogeneity, increases hardness and toughness, and significantly reduces the retained austenite content [15].

2.3.4. Tempering

To achieve the proper toughness-to-hardness ratio, tempering is indispensable. For hot-forming tool steels, high-temperature multiple tempering cycles are necessary to form a fine-grained homogeneous spheroidite structure [16], and to reduce stresses caused by heat treatment.

The final hardness was achieved by adjusting the second tempering temperature. In our case, triple high-temperature tempering was applied.

 Table 2. Heat treatment parameters [1]

Process	Temp. (°C)	Time (min)
Stress relief	650	260
Hardening	1050	200
Cryogenic treatment	-150	145
Tempering 1	605	240
Tempering 2	615	240
Tempering 3	595	240
	Total	ima. 1995 min

BALINIT FORMERA differs from conventional PVD coating. In our experiment, the process began with plasma nitriding, followed by PVD coating. As a result, an adhesive layer of 7 μm and a diffusion layer of 80 μm thickness were created. Nitriding is carried out at 480 °C, and the coating temperature does not exceed the tempering temperature of the tool [17]. BALINIT FORMERA produces a multilayer structure, which significantly reduces crack propagation. Its main advantages include heat resistance up to 1000 °C, reduced adhesion of castings, and high resistance to washout, thereby increasing tool lifetime.

3. Measurement Results

2.4. Surface Treatment

3.1. Microhardness Testing

During the microhardness measurements, care was taken to use only minimal load to avoid exceeding the coating thickness with the indenter. With a load of 0.5 kg, a hardness of 2200 HV was achieved. The uncoated tool had a hardness of 52 HRC, corresponding to approximately 550 HV.

This means that due to surface treatment, surface hardness increased fourfold compared to the uncoated condition.

3.2. Coating Thickness Measurement

The coating thickness was determined using a FISCHERSCOPE® X-RAY XDAL® device, which operates on the principle of X-ray fluorescence (XRF). This method enables non-destructive measurement of coating thickness by evaluating the characteristic fluorescent radiation of the elements in the coating and the substrate.

Measurements were carried out on all three coated samples (Fig. 7) providing precise data on the thickness of each layer. The coating thickness measurement was repeated on the three test specimens, and the results were averaged. The average coating thickness was $6.94~\mu m$.

4. Conclusion

In our investigations, we compared two test specimens subjected to identical heat treatments, with one of them additionally coated with BALIN-IT FORMERA ADVANCED. Microhardness tests and microscopic microstructural examinations were carried out. After completing the laboratory tests, the coating process was implemented in practice on the tool itself.

With the appropriate heat-treatment technology, the tool was capable of producing 280,000 parts. Thanks to the coating, the new tool could produce an additional 80,000 parts, resulting in a total service life of 360,000 parts.

Table 3. Service life comparison

Service life without coating	Service life with coating
280,000 pcs	360,000 pcs

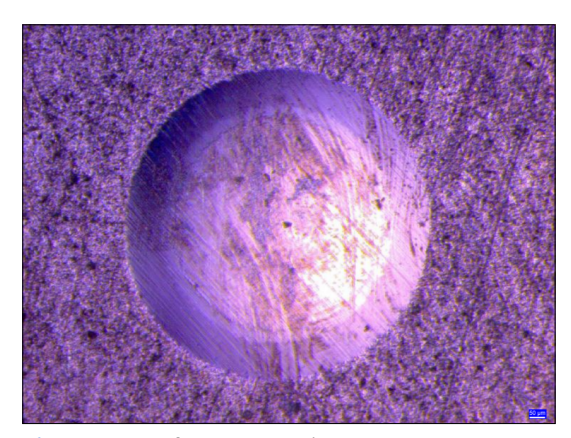


Fig. 7. Image of one test specimen.

Acknowledgements

The authors would like to thank the Faculty of Mechanical and Safety Engineering at Óbuda University, Bánki Donát, for the laboratory facilities, support, and assistance. Further thanks are extended to the Erdélyi Múzeum Egyesület for providing the opportunity to present this topic at the XXX. Scientific Conference of Young Engineers and for supporting the realization of this article.

References

- [1] Kertész O., Tóth L.: Öntőszerszámok élettartamának növelése mélyhűtéses hőkezeléssel. Acta Materalia Transylvanica, 7/2. (2024) 66–70. https://doi.org/10.33923/amt-2024-02-02
- [2] Uddeholm AB: Broshure Uddeholm UNIMAX, 2015.
- [3] Arh B., Podgornik B., Burja J.: Electroslag Remelting: A Process Overview. Materials and Technology, 50/6. (2016) 971–979. https://doi.org/10.17222/mit.2016.108
- [4] Hawryluk M., Lachowicz M., Zwierzchowski M., Janik M., Gronostajski Z., Filipiak J.: Influence of the grade of hot work tool steels and its microstructural features on the durability of punches used in the closed die precision forging of valve forgings made of nickel-chrome steel. Wear, 528–529. (2023) 1–20.
 - https://doi.org/10.1016/j.wear.2023.204963
- [5] Schwam D., Wallace J. F.: Improving Tool Life for Aluminium Die Casting Dies. Die Casting Engineer Reprint, Mar/Apr (1995) 1–4.
- [6] Bitay E., Tóth L., Kovács T. A., Nyikes Z., Gergely A. L.: Experimental Study on the Influence of TiN/AlTiN PVD Layer on the Surface Characteristics of Hot Work Tool Steel. Applied Sciences, 11. (19):9309. (2021) 1–12. https://doi.org/10.3390/app11199309
- [7] Rechverger J., Brunner P., Rubach R.: High performance cutting tools with solids lubricants PVD coatings. Surface and Coating Technologies, 62/1–3. (1993) 393–398. https://doi.org/10.1016/0257-8972(93)90273-Q
- [8] OERLIKON BALZERS: BALINIT bevonatok alkalmazása fémek nyomásos öntésekor. 2020.
- [9] Dúl J.: Nyomásos öntészeti ismeretek 1. kiadás. Nemzeti Tankönyvkiadó, Miskolc, 2009.
- [10] Szabó R.: Öntéstechnikai és hőtechnikai paraméterek hatása az alumínium nyomásos öntvény szilárdsági tulajdonságaira. Doktori értekezés. Miskolci Egyetem Műszaki Anyagtudományi Kar, Miskolc, 2012.
- [11] Azizpour A., Hahn R., Klimashin F. F., Wojcik T., Poursaeidi E., Mayrhofer P. H.: *Deformation and Cracking Mechanism in CrN/TiN Multilayer Coatings*. Coatings, 9(6):363. (2019) 1–17. https://doi.org/10.3390/coatings9060363

[12] Zeghni, A. E.; Hashmi M. S. J.: The effect of coating and nitriding on the wear behaviour of tool steels. Journal of Materials Processing Technology, 155–156. (2004) 1918–1922.

https://doi.org/10.1016/j.jmatprotec.2004.04.281

- [13] Artinger I.: Szerszámacélok és hőkezelésük. Műszaki Könyvkiadó, Budapest, 1978.
- [14] Monah Lal D., Renganarayanan S, Kalanidhi A.: *Cyrogenic treatment to augment wear resistance of tool and die steels.* Cryogenics, 41, 3. (2001) 149–155.

https://doi.org/10.1016/S0011-2275(01)00065-0

[15] Podgornik B., Paulin I., Zajec B., Jacobson S., Leskovšek V.: Deep cryogenic treatment of tool steels. Journal of Materials Processing Technology, 229. (2016) 398–406.

https://doi.org/10.1016/j.jmatprotec.2015.09.045

[16] Tóth L.: Reduction of retained austenite in tool steels. Acta Materalia Transylvanica, 5/2. (2022) 52–57.

https://doi.org/10.33894/mtk-2022.16.10

[17] Zhanga K., Dengb J., Guoa X., Suna L., Leic S.: Study on the adhesion and tribological behavior of PVD TiAlN coatings with a multiscale textured substrate surface. International Journal of Refractory Metals and Hard Materials, 72. (2018) 292–305.

https://doi.org/10.1016/j.ijrmhm.2018.01.003

Acta Materialia Transylvanica 8/1. (2025) 23–27.

DOI: Hungarian: https://doi.org/10.33923/amt-2025-01-05

English: https://doi.org/10.33924/amt-2025-01-05



Tool Development for Friction Stir Welding of Aluminium Alloys

Emese KOZÁK, ¹ Zsolt Ferenc KOVÁCS ²

- ¹ John von Neumann University, GAMF Faculty of Engineering and Computer Science, Department of Innovative Vehicles and Materials, Kecskemét, Hungary. kozak.emese@nje.hu
- ² John von Neumann University, GAMF Faculty of Engineering and Computer Science, Department of Innovative Vehicles and Materials, Kecskemét, Hungary.

Abstract

In recent years, the demand for aluminium and aluminium alloys has increased due to their favourable properties. The properties of aluminium alloys are almost the same as structural steel, but their weight is approximately one third. Technological developments have made it possible to weld metals that are difficult to weld with traditional fusion welding, such as aluminium alloys, using Friction Stir Welding (FSW). This article briefly introduces the FSW procedure and its application. During this research, 5053 aluminium alloys were welded with the mentioned technology, for which customized FSW tools were used. These tools were made with 3D printing technology, which ensured the manufacturing of complex geometries. After welding, the pieces were subjected to the following material tests: visual inspection, tensile tests, hardness tests and metallographic analysis.

Keywords: friction stir welding, FSW tool, aluminium, material testing.

1. Introduction

Friction stir welding (FSW) is a solid-state welding process in which the joint is formed without melting the base materials [1].]. Its basic principle is that a rotating tool is used that penetrates the fixed workpieces to be welded. The shoulder of the tool generates frictional heat, which causes a local decrease in the strength of the workpieces, thereby softening the material. During this stage, the rotating tool moves along the joint line, stirring the plastically deformed material, and upon cooling, a solid-state bond is formed between the workpieces [2, 3, 4].

The main parts of the tool are shown in Fig. 1. Since the illustration from source [5] showed the basic design of the FSW tool with a conceptual error, it has been corrected and republished accordingly.

Variables during the process include the materials to be welded, their quality, thickness, and the number of dissimilar materials to be joined. Technological parameters include the tool inclination angle, transverse speed, rotational speed, axial force applied to hold the tool in the material, and in some cases the presence or absence of cooling.

Key factors in tool design include the tool material, shoulder diameter, and pin geometry, diameter, and length [6, 7, 8, 9].

Additive manufacturing, one of the most dynamically developing manufacturing technologies, also plays an important role in this research. While FSW tools are typically produced by machining (subtractive manufacturing), additive manufacturing becomes an attractive option when the tool requires complex pin and shoulder

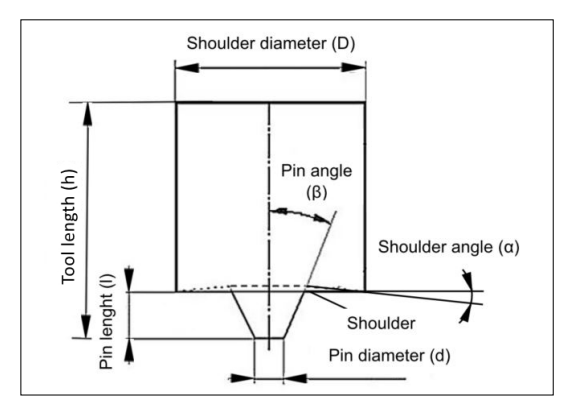


Fig. 1. Simplified schematic of the FSW tool. [5]

geometries that are difficult or impossible to machine. Additive manufacturing enables the production of such complex shapes and also brings economic benefits.

2. Design of the FSW tool

Additive manufacturing of metal parts allows for faster and more cost-effective production of complex geometries compared to traditional machining, including friction stir welding. Additive manufacturing has so far mainly appeared in friction stir welding by welding additively manufactured workpieces together [10]. Therefore, this research can be considered pioneering, as it is the first study in Hungary on the use of additively manufactured friction stir welding tools.

The design was primarily based on the work-pieces to be welded – in this case, two 4 mm thick aluminium plates. The plate thickness determines the length of the pin, which cannot be equal to or greater than the material thickness. The pin should be slightly shorter to avoid full penetration. Consequently, the pin length was set to 3,7 mm.

The shoulder diameter significantly influences the formation of the weld. For aluminium alloys, the shoulder diameter is typically 2,5 to 3 times the pin diameter. The shoulder diameter affects both the weld width and the amount of frictional heat generated.

In this study, all tools were designed with a shoulder diameter of D = 20 mm. However, future work should include testing different shoulder diameters under the same process parameters. The overall tool length was h = 15 mm in all cases, which provides a suitable clamping length and cost-effectiveness in production.

The pin diameter and geometry, as well as the shoulder face and profile, were varied between tools to improve material flow during welding (Fig. 2).

3. Description of Welding Experiments

The base material was aluminum alloy 5053, with specimen dimensions of $50 \times 90 \times 4$ mm. The goal of the research was to identify, under fixed welding parameters, the most suitable tool geometry based on destructive and non-destructive testing of the weld quality.

A total of 15 welds were performed at a constant rotational speed of 1000 min⁻¹, using three different traverse speeds. The tool tilt angle was 0°, and no cooling was applied (Table 1.).

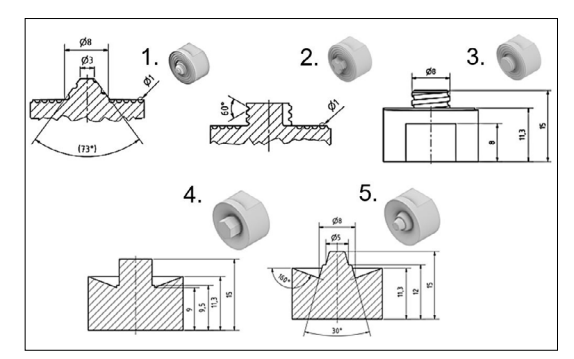


Fig. 2. Designed FSW tools from 1 to 5 with dimensions.

Table 1. Technological parameters of the welding process

p. cccs		
Number of Measurements	Tool Name	Feed v_f (mm/min)
1.		80
2.	1.	125
3.		170
4.		80
5.	2.	125
6.		170
7.		80
8.	3.	125
9.		170
10.		80
11.	4.	125
12.		170
13.		80
14.	5.	125
15.		170

During welding, the plates were positioned in the same plane, and the joint was formed along their contacting edges. Due to the spiral tool design, the spindle rotated counterclockwise (M4 direction) during welding to ensure proper material flow consistent with the tool geometry. The experimental setup is shown in Fig. 3.

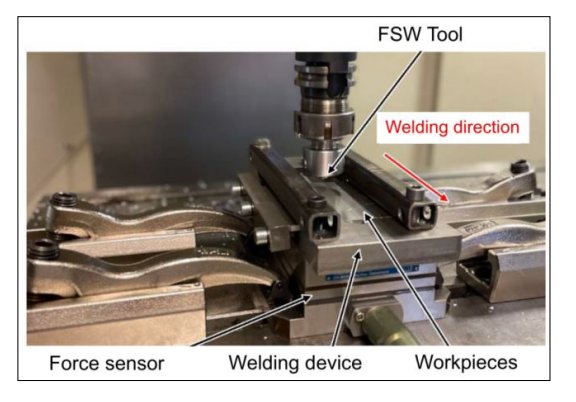
4. Material testing

This chapter summarizes the procedure and results of the evaluation of welded samples. The welds were examined visually, as well as by tensile testing, hardness testing, and metallographic analysis.

4.1. Welding quality by visual inspection

The welds made with tools 1 and 3 are particularly noteworthy.

With tool 1, at a transverse speed of 80 mm/min, the tool "plowed" the material, resulting in insufficient material mixing and poor weld formation. At a speed of 125 mm/min, the quality of the joint improved significantly, but at higher speeds, tunnel-type porosity defects appeared (Fig. 4).



For tool 3, welds were successfully created in all three experiments, although the surface roughness varied. A transverse speed of 80 mm/min produced a rougher surface, while increasing the speed produced smoother welds. However, defects observed at the beginning of the weld are indicative of internal tunnel porosity (Fig. 5).

4.2. Welding quality by tensile test

For transverse tensile tests, three specimens (10 mm wide) were cut from each welded sample. The nominal specimen width was 8 mm and the total length was 98 mm, resulting in a total of 36 specimens, 33 of which were tested at different transverse speeds. The tests were performed using an Instron 4482 tensile testing machine.

The highest tensile strengths were measured for specimens 1/125 and 3/125. The summarized results are shown in Table 2.

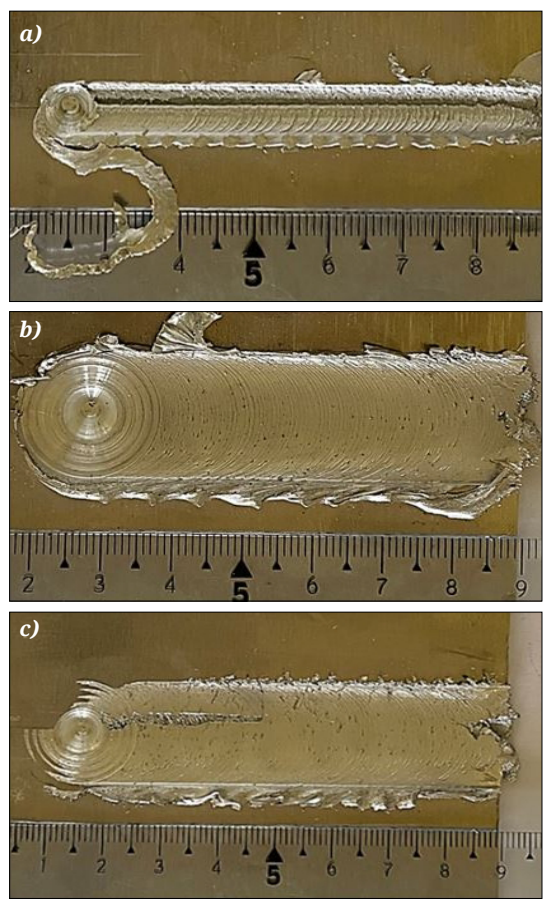


Fig. 4. Top view of welds produced with Tool 1: a) 80 mm/min; b) 125 mm/min; c) 150 mm/min

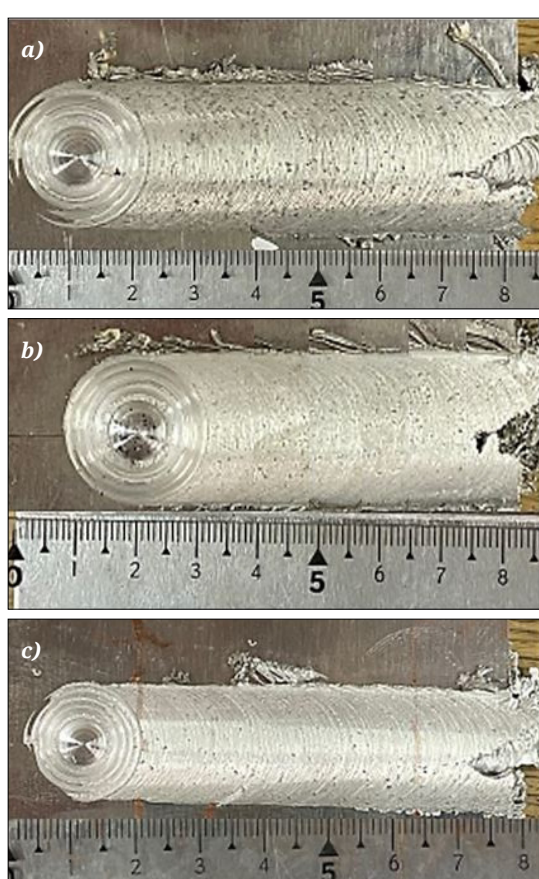


Fig. 5. Top view of welds produced with Tool 3: a) 80 mm/min; b) 125 mm/min; c) 150 mm/min

3/125b

3/125c

Próbatest	Max. terhelés (N)	Megnyúlás max. ter- helésnél (mm)	Szakító- szilárdság (MPa)
1/125a	6869	10,76	215
1/125b	6946	11,63	212
1/125c	6870	10,76	224
3/125a	6111	7,51	186

11.99

13,18

215

214

2. táblázat. A szakítóvizsgálat eredményei (részlet)

4.3. Welding quality by metallographic examination

7060

7109

The cold-embedded samples were sanded in three stages with 320, 600 and 1200 grit sandpaper and then examined under a microscope for internal defects.

Different sizes of defects were found in each weld. The lowest defect incidence was observed in the 1/125 and 3/125 welds (Fig. 6 and 7).

4.4. Welding quality by hardness testing

Vickers hardness measurements were performed on the mounted samples using a Struers Duramin-100 tester. The measurements were carried out on the 1/125 and 3/125 specimens, which had shown the best performance in earlier tests. The applied load was 9.81 N.



Fig. 6. Cross-section of specimen welded by tool 1 at a feed rate of 125 mm/min.

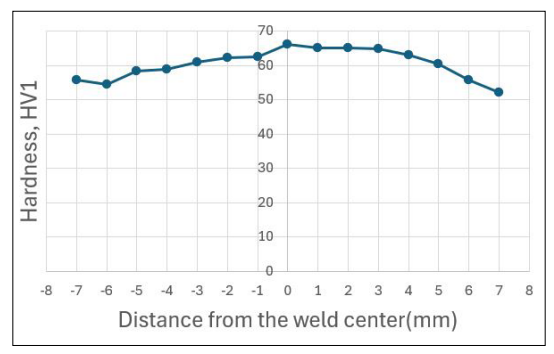


Fig. 8. Hardness measurement of the sample welded by tool 1 at a feed rate of 125 mm/min.

Since the welded plates were made of identical material, the hardness values were expected to be nearly uniform across the measured points, with slightly higher hardness within the weld zone. Measurements were taken along the crown side from the retreating to the advancing side (Fig. 8 and 9) [2].

5. Conclusion

Of the results, welds made with tools 1 and 3 at a travel speed of 125 mm/min were the most promising. These tools should be further tested with different welding parameters, such as different tool inclination angles (1–3°).

The spiral grooves on the tool improved material flow during mixing.

Further research should also investigate concave shoulder designs to empirically determine the optimal shoulder angle that promotes favorable weld formation.

For tool 2, vertical grooves on the pin should be avoided under the test conditions, as this configuration did not give satisfactory results at any travel speed. However, further experiments are recommended, adjusting the groove geometry to ensure material flow along them during welding.

Acknowledgements

The project number 2024-2.1.1-EKÖP-2024-00008 was implemented with the support of the Ministry of



Fig. 7. Cross-section of specimen welded by tool 3 at a feed rate of 125 mm/min.

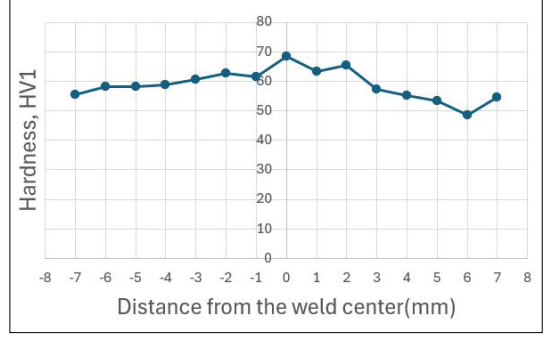


Fig. 9. Hardness measurement of the sample welded by tool 3 at a feed rate of 125 mm/min.

Culture and Innovation from the National Research Development and Innovation Fund, financed by the 2024-2.1.1-EKÖP application program.

References

- [1] Michael H., Stefan B., Sven S.: *Influence of surface roughness of tools on the friction stir welding process.*Journal of Welding and Joining, 32/6. (2014) 22–28. https://doi.org/10.5781/JWJ.2014.32.6.22
- [2] Kovács Zs. F., Hareancz F.: A kavaró dörzshegesztés alkalmazási lehetőségei alumínium kompozitok esetén. Gradus, 8/1. (2021) 294–298. https://doi.org/10.47833/2021.1.ENG.011
- [3] Singh Bharat Raj: *A Hand Book on Friction Stir Welding*. LAP Lambert Academic Publishing, UK, 2012. 3–7, 69, 72–74, 90–104. https://doi.org/10.13140/RG.2.1.5088.6244
- [4] Kilic S., Ozturk F., Demirdogen M. F.: A comprehensive literature review on friction stir welding: Process parameters, joint integrity, and mechanical properties. Journal of Engineering Research, 13/1. (2025) 122–130. https://doi.org/10.1016/j.jer.2023.09.005
- [5] Bilici M. K.: Effect of tool geometry on friction stir spot welding of polypropylene sheets. Express Polymer Letters, 6/10. (2012) 805–807. https://doi.org/10.3144/expresspolymlett.2012.86

- [6] Kovács Zs. F.: Acéllemez kavaró dörzshegesztése. Hegesztés Technika, XXXIV/1. (2023) 51–53.
- [7] Mugada K. K., Kumar A.: Role of Tool Shoulder End Features on Friction Stir Weld Characteristics of 6082 Aluminum Alloy. Journal of The Institution of Engineers (India), Series C, 100 (2019) 343–350.
 - https://doi.org/10.1007/s40032-018-0451-9
- [8] Tarasov S., Amirov A., Chumaevskiy A., Savchenko N., Rubtsov V. E., Ivanov A., Moskvichev E., Kolubaev E.: Friction Stir Welding of Ti-6Al-4V Using a Liquid-Cooled Nickel Superalloy. Tool Technologies, MDPI, 10/118. (2022) 1–2, 13–14. https://doi.org/10.3390/technologies10060118
- [9] Abolusoro O. P., Akinlabi E. T., Kailas S. V.: Impact of tool profile on mechanical behavior and material flow in friction stir welding of dissimilar aluminum alloys. Materialwissenschaft Werkstofftechnic, 51. (2020) 729–730.
- https://doi.org/10.1002/mawe.202000002.
 [10] Javadi M. S., Ehteshamfar M. V., Adibi H.: A comprehensive analysis and prediction of the effect of groove shape and volume fraction of multi-walled carbon nanotubes on the polymer 3D-printed parts in the friction stir welding process. Polymer Testing, 117. (2023), 107844.
 https://doi.org/10.1016/j.polymertesting.2022.

107844.



Acta Materialia Transylvanica 8/1. (2025) 28–33. DOI: Hungarian: https://doi.org/10.33923/amt-2025-01-06 English: https://doi.org/10.33924/amt-2025-01-06



Effect of Laser Surface Hardening on Different Surface Designs in the Case of 1.2379 Tool Steel

Béla MÉSZÁROS, 1 Enikő Réka FÁBIÁN2

- ¹ Óbuda University, Doctoral School on Materials Sciences and Technologies, Budapest, Hungary meszaros.bela@bgk.uni-obuda.hu
- ² Óbuda University, Bánki Donát Faculty of Mechanical and Safety Engineering, Institute of Materials and Manufacturing Sciences, Department of Material Technology. Budapest, Hungary fabian.reka@bgk.uni-obuda.hu

Abstract

Laser surface treatments are increasingly used for the formation of hardened layers. In this experimental series, we examined surfaces machined to three different depths (0.25 mm, 0.5 mm, and 0.75 mm) to determine how these machining depths affect the thickness of the hardened layer. The base material was 1.2379 tool steel in all cases. The focal distance remained constant, while the laser power and scanning speed were varied according to the predefined experimental design. Our results indicate that higher specific power led to a deeper hardened layer. The 45° machining angle—and consequently, the 45° laser beam incidence angle—enhanced absorption and increased the hardening depth. The deepest grooves resulted in the thickest hardened layer. However, during our experiments, certain parameter settings raised the base material's temperature above the liquidus point, causing localized melting.

Keywords: tool steel, laser beam hardening, diode laser, surface texture.

1. Introduction

Diode laser heat treatment plays an increasingly important role in surface hardening within industry, particularly in the automotive, aerospace, and tool manufacturing sectors. The principle of the process is that the laser beam provides localised heat input, which induces a martensitic transformation on the workpiece surface, thereby enhancing wear resistance and service life.

However, the energy absorption and reflection of material surfaces with different topographies have a significant impact on the quality and depth of the hardened layer. Part of the laser radiation is absorbed by the surface of the workpiece, while the remaining portion is reflected, resulting in energy loss. The degree of reflection depends on the wavelength of the applied radiation and on the surface roughness of the workpiece [1]. Due to high reflection, part of the laser radiation cannot be utilised, which may lead to uneven heat input and an inhomogeneous hardened layer. To address this issue, various industrial surface treat-

ment techniques are applied:

- Surface oxidation: A thin oxide layer (e.g. produced by heat treatment or chemical processes) reduces reflection, particularly on polished surfaces.
- Blasting or etching: Producing a rougher surface increases absorbed energy and decreases reflection.
- Application of graphite or paint coatings:
 These materials improve absorptivity and are frequently used in industry prior to laser welding and surface treatments [2].

The different types of lasers operate at different wavelengths, and these operating ranges alter the amount of heat introduced into the material, thereby influencing the thickness of the hardened layer. **Table 1** shows the percentage absorption capacity of different surfaces, i.e. their energy absorptivity, for two types of lasers.

The ${\rm CO}_2$ laser operates in the infrared range (at a wavelength of 10.6 μ m), while the YAG laser typically operates in the near-infrared range (at a wavelength of 1.06 μ m). This difference in wave-

Table 1. Absorption coefficient at different surface
qualities and laser technologies [3]

0 f	Absorption, %	
Surface	Diode laser, 700–1070 nm	
Polished	30–40	
Ground	45–55	
Turned	55–65	
Sandblasted	75–85	
Oxidised	85–95	
Graphite-coated	90–98	

length plays a decisive role in how various materials and surface structures absorb laser radiation. In the case of smooth, polished surfaces, absorption is generally lower, whereas roughened or oxidised surfaces tend to absorb more energy. Regarding absorption parameters, CO2 and YAG lasers behave differently on differently treated surfaces. For polished surfaces, absorption is low for both types of lasers, but YAG laser radiation is absorbed somewhat more effectively by metals, while CO2 laser radiation is more prone to reflection. Ground and turned surfaces already show higher absorption, particularly with the YAG laser, as the fine roughness facilitates energy absorption. Sandblasted and oxidised surfaces exhibit significantly better absorptivity for both lasers, but again the YAG laser proves more efficient. Graphite-coated surfaces demonstrate outstanding absorption in the case of both types of lasers [3].

Based on the absorption values, the YAG laser is more suitable for surface hardening, as its radiation is absorbed more effectively on various metallic surfaces, particularly on oxidised, sandblasted, and graphite-coated layers. The $\rm CO_2$ laser, on the other hand, is more ideal for non-metallic materials and for the heat treatment of larger surfaces. The proper selection of the laser type therefore plays a critical role in achieving optimal heat input and uniform hardening depth.

Diode lasers are widely used laser types, applied in industrial machining, medical devices, and communication systems. These lasers operate within the 700–1070 nm wavelength range, which allows their radiation to be absorbed efficiently by various metallic surfaces, particularly when the surface is oxidised or roughened. In this experimental series, a diode laser was employed, the main advantages of which are its high mobility, ease of operation, and tunability. Table 2

Table 2. Variation of the hardened layer thickness with laser beam incidence angle [2]

Incidence angle	Hardened layer thickness (mm)	
90°	1.2 mm	
60°	0.8 mm	
45°	0.5 mm	

presents the absorption characteristics of diode lasers on different surfaces, expressed as percentages.

The 1.2379 steel (AISI D2) is a cold-work tool steel, for which hardening is essential to increase service life and wear resistance. During diode laser surface hardening, the thickness of the hardened layer typically varies between 0.3 and 1.5 mm, depending on the laser power and the machining speed [4]. The thickness of the hardened layer also depends on additional factors, such as the angle of incidence of the beam. This determines energy absorption and heat distribution. A 90° incidence angle ensures optimal absorption, whereas at smaller angles (e.g. 45°) part of the radiation is deflected from the surface, reducing the efficiency of hardening [5].

In an experiment, diode laser surface hardening of AISI 410 stainless steel was examined at different incidence angles, where the hardened layer thicknesses obtained are shown in **Table 2**, in accordance with the angle of incidence of the beam.

2. Materials, equipment and technologies

The base material was a Ø80 mm hot-rolled, pre-hardened 1.2379 (X153CrMoV12 or D2) tool steel bar (1.53% C, 0.35% Si, 0.4% Mn, 12% Cr and 0.85% V), with a hardness of HB 230–250. For the experiments, slices of 30 mm thickness were cut, and the plane surfaces thus obtained were used for the tests. In order to determine how machining surfaces influence laser hardening, V-shaped grooves of different depths were produced.

Surface preparation of the specimens was carried out on a universal milling machine, where grooves of 0.25, 0.5 and 0.75 mm depth were milled (see Fig. 1). The tool applied was a solid carbide end mill (MC326-12.0W4L050C-WK-40TF) with a main cutting edge angle of 90°. The V-shaped grooves were created by tilting the main spindle and owing to the design of the tool, while an appropriate coolant-lubricant was applied. During the milling operations, ensuring

proper cooling and lubrication was essential for maintaining the quality of the machining process.

Laser heat treatment was carried out at the laser technology plant of Budai Benefit Kft. During the process, a 4 kW diode laser was applied with three different sets of technological parameters.

The aim of the procedure was to investigate the effect of grooves of different depths on laser heat treatment and on the properties of the material. The experimental results contribute to determining the optimal technological parameters for industrial applications. Based on preliminary literature research [2, 6] the specimen surfaces were scanned with specific heat inputs of 150, 200 and 240 Ws/mm. During the surface treatment, a focal distance of 340 mm was used, measured relative to the plane surfaces. The technological data belonging to each specimen designation are shown in Table 3.

The surface-treated specimen was cut 10 mm away from the heat-treated surfaces using a band saw with the application of coolant-lubricant (see Fig. 2). From the resulting plates, strips of 40 mm width were sectioned along the centreline of the heat-treated tracks for metallographic examinations, ensuring that the specimens contained evaluable portions both from the grooved area and from the plane surface.

After cold mounting, the specimens were ground and polished in several stages, and then etched with Nital-2 in order to reveal the hardened layer thicknesses. The optical microscopic analyses were performed using an Olympus DSX1000 digital microscope.

The hardness of the specimens was measured with a Zwick 3212 hardness tester, both perpendicular to the plane surface and starting from the tip of the grooves. In order to measure hardness variations while maintaining the prescribed spacing between indentations [7], the applied load was selected as 1.962 N.

3. Experimental results

Our conclusions were drawn from microscopic analyses of the prepared cross-sections and from the hardness profiles measured on the specimens.

The preliminary literature research [6], and the metallographic examinations show that the thickness of the hardened layer is smaller than at the machined surfaces. It can be observed that even at the lowest specific energy input, the sharp peaks and valleys of the machined V-shaped grooves lost their form, and rounded shapes be-

Table 3. Technological data for each specimen

Set parameters	Specimen number and corresponding machining depth		
	0.25 mm	0.5 mm	0.75 mm
1.2 kW → 8 mm/s	22	23	24
1.6 kW → 8 mm/s	25	26	27
1.2 kW → 5 mm/s	28	29	30

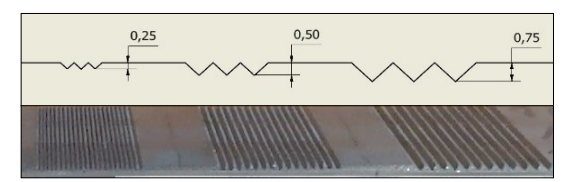


Fig. 1. Schematic and image of the prepared surfaces.

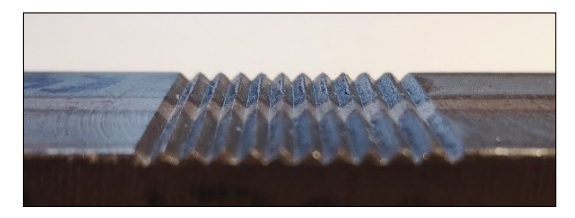


Fig. 2. Grooves of 0.75 mm depth after heat treatment.

gan to appear (Fig. 3). The originally produced shape is indicated by a red line in Fig. 3. In this experimental series, this setting represented the condition where the least amount of heat was introduced into the base material.

To reveal the hardness variation, hardness measurements were performed both perpendicular to the plane surface and starting from the edges of the machined grooves. Based on the data thus obtained, hardness variation diagrams were constructed.

The highest hardness values were typically measured in the hardened surface layer, gradually decreasing towards the core. The hardness measurement results obtained with the lowest heat input are shown in Fig. 4.

The hardness measurements show that at the machined peaks the hardness of the hardened layer is higher than in the vicinity of the plane surface. This indicates that greater heat absorption occurred at the machined edges, which may have contributed to the increase in primary aus-



Fig. 3. Effect of surface heat treatment with a specific heat input of 150 Ws/mm on specimen 22.

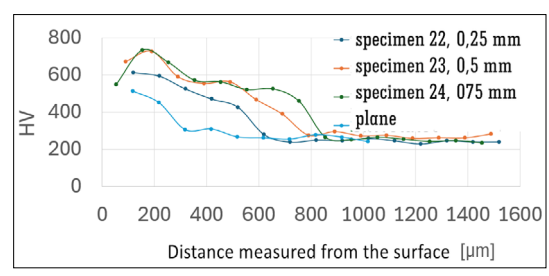


Fig. 4. Hardness variation after heat treatment with a specific heat input of 150 Ws/mm.

tenite grain size. The hardness measurement results (**Fig. 4**) also reveal that, in specimens with deeper grooves, the hardness close to the surface at the machined peaks is lower than at 200 μ m from the surface, a phenomenon that is also reflected in the microstructure (**Fig. 5**).

In the next experimental setting, the laser power was increased from 1200 W to 1600 W, while the scanning speed was kept constant (8 mm/s). As a result of this adjustment, the specific heat input increased to 200 Ws/mm compared with the previous setting. Metallographic examinations revealed that the peaks formed by machining became rounded and partially melted. At low magnification, following etching with Nital, the melted and resolidified regions appear bright (Fig. 6). At higher magnification, dendritic solidification is also clearly visible (Fig. 7). Beneath the melted regions, two transitional zones can be identified. Directly under the melted zone, a region can be observed where the temperature rose between the solidus and Acm, in which homogenisation of the original carbide network structure began. However, due to the short duration of surface treatment, the microstructure did not become homogeneous. In the central region shown in Fig. 6 heating occurred between A1 and Acm, and due to rapid cooling of the specimen, martensitic transformation took place in the areas between the carbide networks. This conclusion is supported by the hardness measurement results shown in Fig. 8. At a depth of 400–600 µm from the surface, the material hardness reached values of

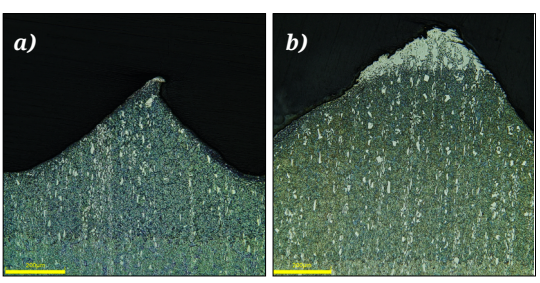
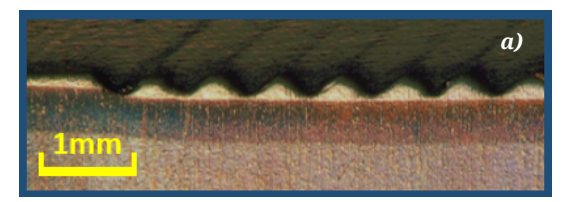
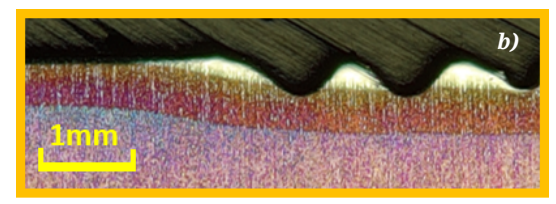


Fig. 5. Vicinity of the machined peak after surface treatment. a) specimen 22 b) specimen 24.





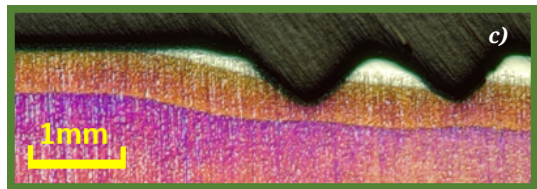


Fig. 6. Cross-sectional appearance of surface heat treatment with a specific beam energy of 200 Ws/mm a) specimen 25 b) specimen 26 c) specimen 27.

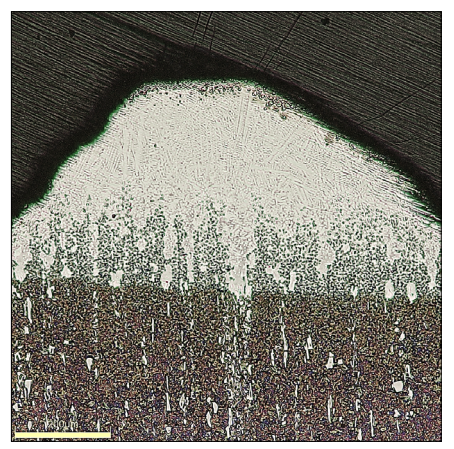


Fig. 7. Vicinity of the machined peak after surface treatment. Specimen 26.

700–750 HV in the grooved regions of 0.5 mm and 0.75 mm depth..

In our final measurement series, we applied a scanning speed of 5 mm/s to the original power of 1200 W, thereby further increasing the specific heat input, so that the plane surface was exposed to a radiation energy of 240 Ws/mm. In this case, the amount of heat transferred into the surface of the base material was sufficient to melt it at the machined peaks (Fig. 9), Consequently, the hardness of the material at these locations was significantly lower than in the regions where only surface hardening occurred, as illustrated in Fig. 10.

The hardness variation diagrams show that in the near-surface region the hardness starts at 500 HV, and as the distance from the surface increases, a harder layer (800 HV) forms at a depth of $450 \,\mu m$ (Fig. 10).

Fig. 9. clearly demonstrates that due to the applied heat input the sharp corners melted, resulting in completely distorted, rounded shapes in the profile.

Inappropriate selection of parameters during the heat treatment of the base material may even cause melting, which, in addition to leading to inadequate surface hardness and wear resistance, can also deform the machined edges—a factor that results in non-conformity in the case of a cold-working tool.

4. Conclusions

In our laser hardening experiments, the behaviour of 1.2379 cold-work tool steel was examined under three different settings with various surface designs. In all cases, the deepest machining depth (0.75 mm) resulted in the deepest hardened layer. The thinnest hardened layer was consistently formed on the plane surface. A laser beam incidence angle of 45° produced higher heat input than perpendicular irradiation.

Where localised melting occurred near the surface due to the surface geometry of the product, dendritic crystallisation developed. The hardness in these regions was lower than in areas where only a martensitic heat-treated microstructure was formed.

For diode laser heat treatment of 1.2379 tool steel, machining depths of 0.5 mm with a 45° inclination still produced a homogeneous hardened layer at a power of 1200 W and a scanning speed of 8 mm/s. At higher energy inputs, however, surface melting may occur, particularly in the vicinity of carbide networks.

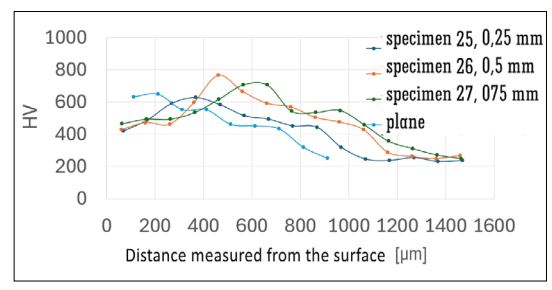


Fig. 8. Hardness profiles after heat treatment with a specific energy of 200 Ws/mm.

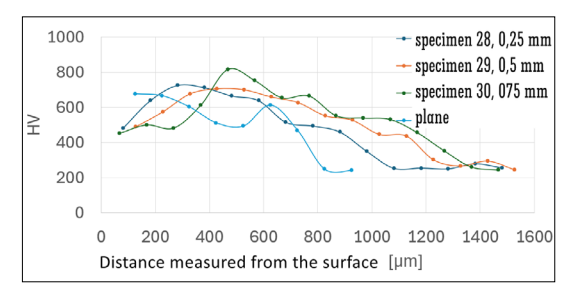


Fig. 9. Hardness profiles after heat treatment with a specific heat input of 240 Ws/mm.



Fig. 10. Cross-sectional appearance of surface heat treatment with a specific heat input of 240 Ws/mm, specimen 30.

References

[1] Henrikki P., Veli K.: Diode laser beam absorption in laser transformation hardening of low alloy steels. Journal of Laser Applications, 16/3. (2004) 147–153.

https://doi.org/10.2351/1.1710879

[2] Moradi M., Arabi H., Jamshidi N, Benyounis K.: A comparative study of laser surface hardening of AISI 410 and 420 martensitic stainless steels by using diode laser. Optics & Laser Technology, 111. (2019) 347–357.

https://doi.org/10.1016/j.optlastec.2018.10.013

- [3] Buza G: *Lézersugaras technológiák I.* Kézirat. Edutus Főiskola, Tatabánya, 2012.
- [4] Temmler A., Cortina M., Ross I., Küpper M. E., Rittinghaus S. K.: Evolution of Surface Topography and Microstructure in Laser Polishing of Cold Work Steel 1.2379 (AISI D2) Using Quadratic, Top-

- Hat Shaped Intensity Distributions. Materials, 15/3. (2022) 769. https://doi.org/10.3390/ma15030769
- [5] Dewi H. S., Volp J., Kaplan A. F. H.: Leaser beam absorbtion depending on the angle of incidence on groud surfaces. Laser in manufacturing conference LIM 2019. 1–6. pdf.
- [6] Mészáros B., Fábián E. R.: The Effect of Surface Machining Design on the Efficiency of Laser Surface Treatment. Acta Materialia Transylvanica, 7/2. (2024) 88–93.
 - https://doi.org/10.33924/amt-2024-02-06
- [7] MSZ EN ISO 6507-1:2024 Fémek. Vickers-keménységmérés. Mérési eljárás, 2024.



Acta Materialia Transylvanica 8/1. (2025) 34–37.

DOI: Hungarian: https://doi.org/10.33923/amt-2025-01-07

English: https://doi.org/10.33924/amt-2025-01-07



The Effects of the Laser Pulse Duty and the Wobble in Case of Manual Laser Welding

Virág SIMON,¹ Balázs VARBAI,² Zsolt PUSKÁS³

- ¹ Budapest University of Technology and Economics, Faculty of Mechanical Engineering, Department of Materials Science and Engineering, Budapest, Hungary, simon.virag240@gmail.com
- ² Budapest University of Technology and Economics, Faculty of Mechanical Engineering, Department of Materials Science and Engineering, Budapest, Hungary, varbai.balazs@gpk.bme.hu
- ³ Exasol Kft. Rétság, Hungary, puskas@exasol.hu

Abstract

In our research we investigated the effects of the laser pulse duty and the wobble on the weld geometry in pulsed mode manual laser welding. Our experiments showed that, for the parameters studied, complete fusion can be achieved without laser wobbling at 500 W power for a material grade of 1.4301 and a wall thickness of 1.4 mm. Increasing the laser wobble amplitude led to an increase in weld width and a decrease in weld depth and weld area. Increasing the pulse duty also increased the weld width, weld depth and weld area. Without laser wobbling, a weld with an area of 1.1 mm² was produced when the pulse duty was set to 70%, while a weld with an area of 1.6 mm² was produced when the pulse duty was set to 100%, so that the area of the weld welded with a pulse duty of 70% was approximately 70% of the area of the weld welded with a pulse duty of 100%.

Keywords: manual laser welding, pulsed laser, pulse duty, laser wobble, weld geometry.

1. Introduction

The mechanised version of laser welding is widely used in the industry because of its many advantages [1]. The highly concentrated laser beam, focused on a small area, creates a very low heat-affected zone and results in low heat input compared to conventional fusion welding processes, minimizing deformation and warpage of the workpiece due to internal stresses [2, 3]. Another advantage of laser welding is that it offers high processing speeds and thus high productivity [4]. Handheld laser welding equipment, which has been introduced in recent years, is becoming increasingly common, and more and more companies are also selling and using such equipment in Hungary. The user-friendly operation provided by the lightweight welding gun and working cable, as well as the small size of the mobile laser oscillator, makes these welding machines increasingly popular [5]. However, due to its novelty, relatively little experience and research is available on this process compared to older, traditional welding processes.

In the present study, we investigated the effects of the laser pulse duty and the wobble on the weld geometry in case of manual laser welding of austenitic stainless steel.

2. Welding and evaluation procedure

Our series of experiments consisted of 12 beadon-plate welds. The experimental welds were made on 1.4301 grade austenitic stainless steel tubes of 1.4 mm wall thickness and 34 mm outer diameter by manual laser welding. No filler material was used.

During the preparation of the welds, the handheld laser welding gun was clamped in the device to ensure its stability, thus minimising errors due to the instability of the human hand. Uniform travel speed was ensured by rotating the workpiece by a rotary motion. The percentage chemical composition of the used steel is shown in Table 1 according to EN 10088-1:2014.

Table 1. The percentage chemical composition of 1.4301 grade austenitic stainless steel [6]

С	Si	Mn	P	S
≤0.07	≤1.00	≤2.00	≤0.045	≤0.015
N	Cr	Ni	Fe	
≤0.11	17.5–19.5	8.0–10.5	mar.	

The experimental welds were made on a Light-WELD XC type, optical fibre, hand-held welding machine, manufactured by IPG Photonics Corporation of the USA. The welding machine is capable of producing a monochrome, coherent and low divergence laser beam with a maximum power of 1500 W and a wavelength of 1080 nm. An online, computer-accessible control interface provides the possibility to adjust the laser power, the wobble width and frequency, the pulse frequency and the pulse duty in pulsed mode. In pulsed mode, the pulse frequency is the number of pulses per second emitted by the laser oscillator and the pulse duty expresses the ratio between the pulse duration and the time elapsed from the start of one pulse to the start of the next, in percentage form. In our experiments, the travel speed (v) was 80 cm/min and the laser power (P) was 500 W. The energy input was calculated using the following formula:

$$E = \frac{P(kW)}{v\left(\frac{mm}{s}\right)} = \frac{0.5}{13.33} = 0.0375 \frac{kJ}{mm}$$
 (1)

The shielding gas used was nitrogen of 4.5 purity at a flow rate of 18 l/min. The pulse duty was varied between 70% and 100% at 10% intervals, and the laser wobble amplitude was set between 0 mm (i.e. the case without wobbling) and 2 mm. Both the pulse frequency and the wobble frequency were 200 Hz for the 1 mm and 2 mm cases. Laser wobbling is performed inside the welding gun by an optically refractive oscillatory motion of the laser beam [7].

At the end of the welding experiments, metallographic grindings were made from the test specimens using conventional methods. The weld shapes were made visible by etching. The etching was carried out using Adler etchant of the following composition:

- 9 g copper ammonium chloride;
- 150 ml hydrochloric acid;
- 45 g ferric chloride 6-hydrate;
- 75 ml distilled water.

The shape of the welds were made successfully visible by etching at room temperature for 4-5 seconds, which were examined with an Olympus SZX 16 stereomicroscope. Microscopic images of the welds were taken to measure the weld width, weld depth and weld area dimensions for evaluation.

3. Results and evaluation

Fig. 1 illustrates the resulting weld width as a function of the laser pulse duty and the wobble amplitude. It can be observed that the width of

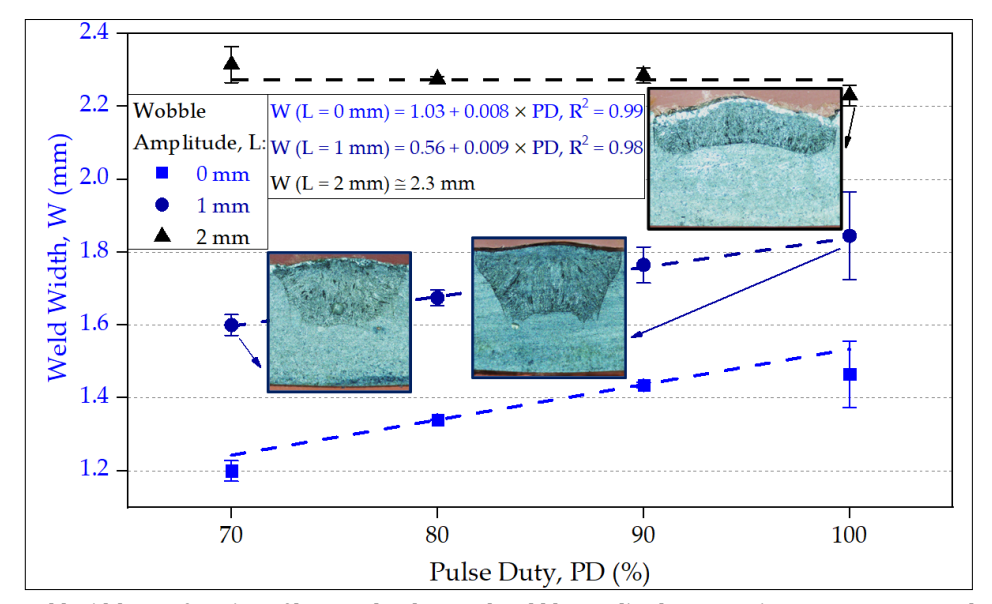


Fig. 1. Weld width as a function of laser pulse duty and wobble amplitude, energy input was $E = 0.0375 \, kJ/mm$.

the welds made with a 2 mm wobble amplitude became nearly constant, while the weld width increased almost linearly with increasing the pulse duty for the 1 mm wobble amplitude and no laser wobble cases. Increasing the wobble amplitude led to an increase in weld width.

Fig. 2. shows the weld depth as a function of the laser pulse duty and the wobble amplitude. It can be observed that the weld depth increases al-

most linearly with increasing pulse duty for both 2 mm and 1 mm wobble amplitude. It can also be concluded that for welds prepared without laser wobble, the weld depth is approximately the same, since in these cases a fully penetrated weld is formed.

Fig. 3 plots the weld area as a function of the parameters tested. The diagram shows that the area of the welds increases almost linearly with the in-

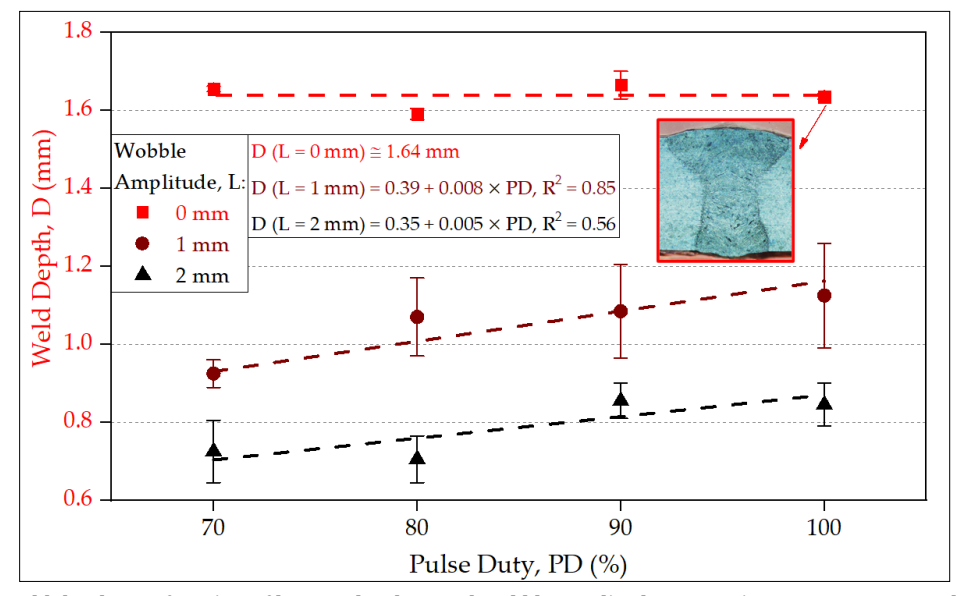


Fig. 2. Weld depth as a function of laser pulse duty and wobble amplitude, energy input was E = 0.0375 kJ/m.

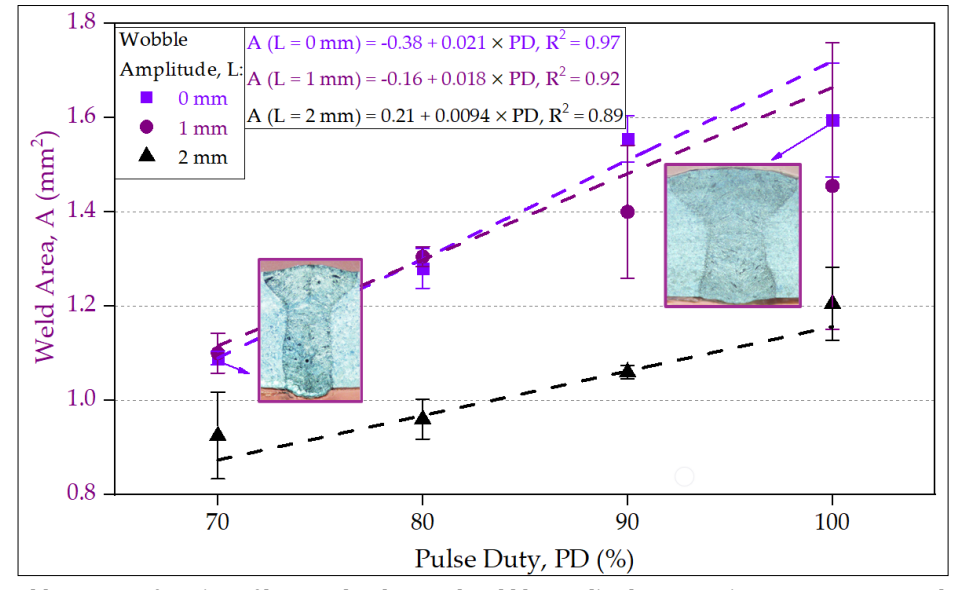


Fig. 3. Weld area as a function of laser pulse duty and wobble amplitude, energy input was $E = 0.0375 \, kJ/mm$.

crease of the pulse duty in the case without laser wobble, and also in the case of 1 mm and 2 mm wobble amplitude. This is clearly shown in the two micrographs pasted on the slide. By comparing the values of the weld area of these welds, it can be concluded that without wobbling the laser beam and with the 70% laser pulse duty setting, a weld of 1.1 mm² was obtained, while with the 100% pulse duty setting, a weld of 1.6 mm² was obtained. It is interesting to note that 1.1 mm² is approximately 70% of 1.6 mm², so the area of the weld welded without laser wobble and with 100% pulse duty is 70% of the area of the weld with 70% pulse duty.

4. Conclusions

In the present study, bead-on-plate welds were welded by manual laser welding on stainless steel tubes to investigate the effect of the laser pulse duty and the wobble on the weld geometry. Based on our results, the following conclusions can be drawn:

- at the parameters tested, full penetration was only achieved without laser wobble;
- increasing the laser wobble amplitude increases the weld width, but decreases the weld depth and the weld area;
- all three geometric dimensions of the welds increase as the pulse duty increases;
- in the case without laser wobble, the area of the weld welded with a pulse duty of 70% was 70% of the area of the weld welded with a pulse duty of 100%.

Acknowledgement

Exasol Kft. provided the necessary materials, equipment and tools for the research work, and we thank them for their support. The author's participation in the conference was supported by the Foundation for Mechanical Engineering Education and the Department of Materials Science and Engineering of BME.

References

- [1] Buza G.: Lézersugaras technológiák I. Edutus Főiskola, Tatabánya, 2012. 75.
- [2] Bitay E.: Hegesztési alapismeretek. Erdélyi Múzeum-Egyesület, Kolozsvár, 2021. 58. https://doi.org/10.36242/mtf-16
- [3] Klimpel A., Lisiecki A.: Laser welding of butt joints of austenitic stainless steel AISI 321. Journal of Achievements of Materials and Manufacturing Engineering, 25/1. (2007) 1.
- [4] ESAB Kft., Lézersugaras hegesztés. https://esab.com/hu/eur_hu/esab-university/ blogs/what-is-laser-welding-and-how-does-thetechnique-work/ (letöltve: 2025. február 25.).
- [5] Gapontsev V., Stukalin F., Pinard A., Shkurikhin O., Grapov Y., Markushov I.: Handheld laser welding and cleaning system for typical metal fabrication using 1.5 kW fiber laser source. Proceedings Volume 11981, Fiber Lasers XIX: Technology and Systems. (2022) 1.
 - https://doi.org/10.1117/12.2616585
- [6] EN 10088-1: Stainless steels. List of stainless steels, 2014.
- [7] Sanati S., Nabavi S. F., Esmaili R., Farshidianfar A., Dalir H.: A Comprehensive Review of Laser Wobble Welding Processes in Metal Materials: Processing Parameters and Practical Applications. Lasers in Manufacturing and Materials Processing, 11/2. (2024) 1–37.

https://doi.org/10.1007/s40516-024-00245-w



Acta Materialia Transylvanica 8/1. (2025) 38–42.

DOI: Hungarian: https://doi.org/10.33923/amt-2025-01-08

ENglish: https://doi.org/10.33924/amt-2025-01-08



Sustainability Layer by Layer: Combining Liapor and Cellulose-Based Insulation in a Facade Wall Panel

Dorina SZENDI,¹ Sándor TÁRKÁNYI,² Balázs KÓSA³

- ¹ University of Sopron, Faculty of Wood Engineering and Creative Industries, Cziráki József Doctoral School of Wood Sciences and Technologies, Sopron, Hungary, VSWIGW@uni-sopron.hu
- ² University of Sopron, Faculty of Wood Engineering and Creative Industries, Institute of Creative Industries, Sopron, Hungary, tarkanyi.sandor@uni-sopron.hu
- ³ University of Sopron, Faculty of Wood Engineering and Creative Industries, Institute of Creative Industries, Sopron, Hungary, kosa.balazs@uni-sopron.hu

Abstract

The combination of Liapor lightweight concrete wall panels and cellulose-based insulation materials represents an outstanding example of the construction industry's commitment to sustainability. The aim of this research is to present the layered integration of Liapor technology and natural-based insulation materials, combining energy efficiency with the principles of eco-conscious architecture. As a result of this integration, an innovative building structure is created, which significantly reduces the energy consumption of buildings, meets passive house standards, and provides excellent acoustic properties.

Keywords: Liapor, cellulose, sustainability, energy efficiency, layered integration, passive house.

1. Introduction

Global climate change, the depletion of natural resources, and the growing societal demand for sustainability have brought significant changes to the world of architecture and the construction industry. The built environment is no longer judged solely by functionality and aesthetics. Energy efficiency, the sustainability of material use, and the minimization of ecological footprint have also become key priorities.

The production and use of traditional building materials result in considerable environmental impact, including high carbon dioxide emissions and the generation of large amounts of waste [1]. The United Nations Sustainable Development Goals (SDGs) clearly emphasize the need to prioritize green technologies in construction. The use of prefabricated building elements, as well as the integration of natural and recycled materials, plays a crucial role in reducing environmental impact [2].

The use of Liapor lightweight concrete wall panels and cellulose-based insulation materials offers an innovative solution that not only supports sustainability principles but also contributes to improved energy efficiency and reduced construction time [3]. The aim of the research is to investigate the integration possibilities of these materials, with particular focus on structural stability, thermal and acoustic insulation properties, as well as their impact on construction costs.

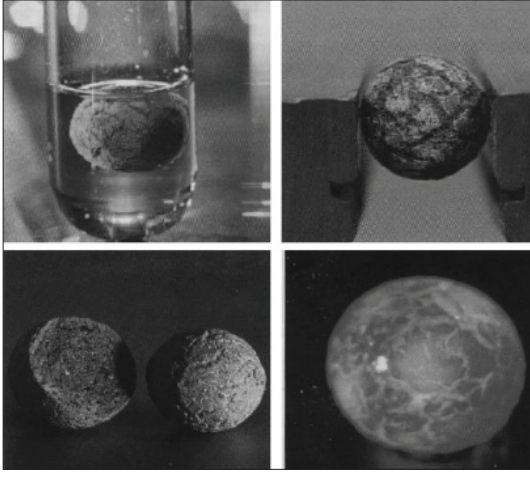


Fig. 1. Microscopic examination of Liapor ceramic test samples

2. Materials and Methods

The aim of the research is to examine the integration of Liapor lightweight concrete wall panels and cellulose-based insulation materials, with particular focus on structural stability, thermal and acoustic insulation properties, and sustainability aspects. The applied methodology consisted of several steps, including material testing, laboratory experiments, and comparative analyses.

The main component of the examined Liapor panels is expanded clay granulate, which, despite its low bulk density (500–600 kg/m³), possesses significant compressive strength, reaching values of 6–8 N/mm². The porous structure contributes to a low thermal conductivity coefficient (approximately 0.12 W/m·K).

Cellulose insulation materials are of natural origin, produced from by-products of the wood industry such as sawdust and poplar bark. Their density ranges from 35–70 kg/m³, with a thermal conductivity coefficient in the range of 0.038–0.045 W/m·K, resulting in excellent insulating properties.

During the research, various layer combinations were tested. The laboratory measurements focused on the following properties:

Thermal conductivity: When Liapor and cellulose insulation were used together, the average thermal conductivity of the layer structure was $0.065\,\mathrm{W/m\cdot K}$, which significantly reduces heat loss.

Compressive strength: According to tests carried out based on the MSZ EN 826 standard, the com-

pressive strength of the cellulose panels ranged between 110–140 kPa, ensuring adequate mechanical stability.

Fire resistance: Based on flammability tests conducted in accordance with the ISO 11925-2 standard, the cellulose panels received a fire resistance rating of D-s1, d0, which provides adequate protection in case of fire.

Vapour diffusion resistance: The μ value ranged between 2 and 5, indicating good breathability and ensuring the proper hygrothermal behaviour of the structure.

Acoustic properties: Sound absorption tests conducted at a frequency of 500 Hz showed that the integrated wall panel achieved an NRC value of 0.75, offering excellent noise reduction capabilities.

As a result of the material tests, it was concluded that the combined use of Liapor lightweight concrete and cellulose-based insulation materials not only increases the energy efficiency of buildings but also contributes to extending their lifespan. Cellulose-based insulation is highly suitable for meeting thermal insulation requirements while also ensuring vapor permeability, which is essential for maintaining the long-term structural stability of buildings.

The applied manufacturing technology allows for the rapid and efficient installation of prefabricated elements, minimizing construction waste and reducing building time. In the construction industry, the use of prefabricated technologies is particularly important for optimizing material usage and increasing energy efficiency [4].



Fig. 2. Liapor wall structure with cellulose insulation

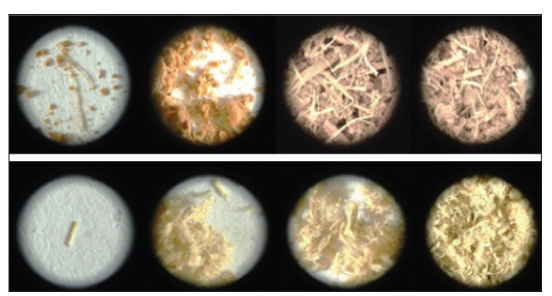


Fig. 3. Microscopic examination of poplar bark fiber and oak fiber



Fig. 4. Cellulose molecule, visibly containing a large number of hydroxyl groups (https://www.ttko. hu/kbf/tan-anyagok_html/kem_38b/index.html)

The research analyzed the forming and density parameters of the developed insulation materials to optimize mechanical resistance and thermal performance. The fiberization technology used in the production of cellulose-based insulation panels ensures a uniform material structure, which is crucial for durability and efficiency. Based on the results achieved, the application of the system offers a promising alternative for sustainable building materials not only in new constructions but also in building renovations [5].

The thermal conductivity of cellulose-based insulation panels is approximately 0.05 W/m²K, which results in outstanding thermal insulation properties and represents a competitive alternative to traditional mineral wool and polystyrene-based insulation materials. The mechanical stability and flexibility of the material were tested using various compression resistance and load tests, which demonstrated that cellulose blocks provide long service life and high strength even under traditional construction use.

The research highlighted that the combination of cellulose-based insulation materials and Liapor wall panels can contribute to improving the sustainability of buildings by reducing energy consumption and the ecological footprint of construction. Such systems may be especially beneficial in the construction of passive houses, where minimal energy consumption and excellent thermal insulation properties are essential requirements [6].

Various building materials and technologies were examined during the research in terms of sustainability, energy efficiency, and structural stability. The main component of Liapor panels is expanded clay granulate, which provides a lightweight yet high-strength structure. Cellulose-based insulation materials were produced from various wood industry by-products such as sawdust and bark fibers, taking into account their thermal and mechanical properties.

The forming and density parameters of the developed insulation materials were also analyzed to optimize mechanical resistance and thermal performance. The fiberization technology used in the production of cellulose-based insulation panels ensures a uniform material structure, which is essential for durability and efficiency. Based on the results achieved, the system provides a promising alternative for the sustainable building materials market not only in new constructions but also in renovations. Liapor technology involves the use of lightweight concrete wall panels that,

due to their porous structure, possess excellent thermal insulation properties. The combination of these panels with cellulose-based insulation materials results in an innovative architectural solution that ensures high energy efficiency and sustainability.

3. Results and Evaluation

Based on the results of the measurements carried out during the research, it can be concluded that the combination of Liapor lightweight concrete and cellulose-based insulation materials led to significant improvements in the thermal and acoustic insulation properties, mechanical strength, and fire resistance of the building materials.

3.1. Thermal Conductivity

Based on the thermal conductivity tests, it was determined that the value for the Liapor and cellulose combination was 0.065 W/m·K, which is lower than that of the Agepan product (0.09 W/m·K). This lower value indicates that the examined layer structure is more resistant to heat loss, thereby supporting building energy efficiency more effectively. The porous structure and the combination of materials reduce the formation of thermal bridges, thus optimizing the thermal performance of buildings in the long term [7].

3.2. Compressive Strength

According to tests conducted in compliance with the MSZ EN 826 standard, the cellulose panels demonstrated a compressive strength ranging between 110–140 kPa, which is more favorable than that of the Agepan panels available on the market (100–120 kPa). This means that the cellulose and Liapor layer structure possesses greater mechanical resistance, enabling the creation of more stable and durable building components. Based on the results, the system offers better resistance to compressive loads, thereby ensuring greater structural integrity [8].

3.3. Fire Resistance

According to tests carried out in accordance with the ISO 11925-2 standard, the cellulose panels received a fire resistance rating of D-s1, d0, while the Agepan panels were rated only E. This indicates that the examined combination is more resistant to fire exposure, ignites more slowly, and emits fewer combustible substances. Due to its higher fire safety, this building material is particularly suitable for residential buildings [9].

3.4. Vapour Diffusion Resistance

During the tests, the μ value of the layer structure ranged between 2 and 5, which ensures optimal hygrothermal properties. In comparison, the Agepan panels showed a lower value (1.8–3), indicating that the Liapor-cellulose combination manages moisture more effectively. This is particularly important in buildings where proper moisture regulation is essential for structural durability and indoor comfort.

3.5. Acoustic Properties

Based on sound absorption tests conducted at a frequency of 500 Hz, the integrated wall panel achieved an NRC value of 0.75, whereas the Agepan panels reached only 0.55 NRC. This means that the Liapor-cellulose combination more effectively reduces noise pollution, which can be especially beneficial in residential buildings.

The results clearly demonstrate that the layered integration of Liapor and cellulose-based building materials not only increases energy efficiency but also contributes to structural stability and sustainable construction solutions. The higher mechanical resistance, more favorable hygrothermal properties, and improved fire safety all confirm that this material combination offers a reliable and competitive alternative for the construction industry in the long term.

4. Conclusions

The combination of Liapor lightweight concrete wall panels and cellulose-based insulation materials provides a promising foundation for the development of sustainable architectural solutions [10]. The results so far have shown numerous advantages, particularly in terms of thermal in-

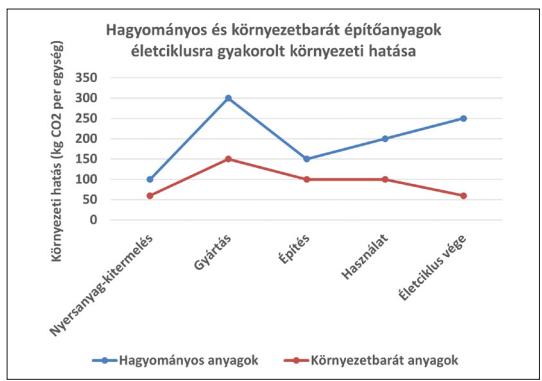


Fig. 5. Lifecycle of Traditional and Eco-Friendly Building Materials.

sulation, mechanical stability, and fire resistance. Research has confirmed that this material combination effectively reduces the energy consumption of buildings while increasing their lifespan and safety.

One of the most important directions for future research is the optimization of layered integration to better exploit the interactions between individual materials. Special attention should be paid to the recycling possibilities of cellulose insulation materials, especially the management of waste generated during building demolition, which can contribute to the development of a circular economy in the construction industry [11].

It is also worth further investigating the adaptability of the Liapor and cellulose combination to various climatic conditions, thus improving its capacity to cope with extreme temperature and humidity fluctuations. The incorporation of building simulation models could also make it possible to predict the energy efficiency and structural behavior of layered configurations already during the design phase [12].

In summary, the combination of Liapor technology and cellulose-based insulation materials represents a significant advancement in the field of sustainable architecture. Further research into new technological developments and material combinations will not only support the advancement of the construction industry but also contribute in the long term to climate protection and the proliferation of energy-efficient construction solutions.

References

- [1] Ertsey A., Medgyasszay P.: Fenntartható építészet. TERC Kiadó, Budapest, 2017. ISBN: 978-6155445422.
- [2] Bozsaky D.: Természetes és mesterséges hőszigetelő anyagok összehasonlító vizsgálatai és elemzése. PhD-disszertáció. Széchenyi István Egyetem, Győr, 2011. 17–22.
- [3] Halász A.: Liapor, a jövő építőanyaga. Magyar Építéstechnika, 41/10. (2003) 11. ISSN: 1216-6022.
- [4] Borzák Balarám B.: Liapor könnyű készbeton. Magyar Építéstechnika, 42/10. (2004) 35. ISSN 1216-6022.
- [5] Mohácsiné Ronyecz I.: Természetes fakéreg anyagok hőszigetelési tulajdonságainak vizsgálata és fejlesztése, 2015. 75–77.
- [6] Ece N.: Building Biology Criteria and Architectural Design. Birkhäuser, Basel–Berlin, 2018. ISBN 978-3-0356-1040-6.
- [7] Mészáros Zs.: Új építőanyagok. MM Műszaki Magazin, 18/7–8. (2008) 8. ISSN 1417-0132.
- [8] Törőcsik N.: A könnyűbeton: a hőszigetelés és hő-

- *védelem régi-új technológiája*. Építési Piac Gyorsjelentés, 38/6. (2004) 59–62. ISSN 1218-0084.
- [9] Burger B., Joób F. T.: LIAPOR kerámiagyöngy. Magyar Építéstechnika, 33/4. (1995) 31. (1. bekezdés). ISSN 1216-6022.
- [10] Benyus J. M.: *Biomimicry: Innovation Inspired by Nature*. William Morrow Paperbacks, New York, 2002. ISBN 978-0060533229.
- [11] Németh K. (1998): *A faanyag degradációja*. Mezőgazdasági Szaktudás Kiadó, Papíripari műszaki-gazdasági tájékoztató, Papíripari vállalat kutató intézet (1980/5.), 93–97.
- [12] Molnár S.: Magyarországi erdők fafajcsoport megoszlása. In: Fahasznosítás Magyarországon. NYME Kiadvány, Sopron, 2008. 78.



Acta Materialia Transylvanica 8/1. (2025) 43–46.

DOI: Hungarian: https://doi.org/10.33923/amt-2025-01-09

English: https://doi.org/10.33924/amt-2025-01-09



An Alternative Process for the Production of Oriented Fibre Reinforced Syntactic Metal Foams

Benedek SZOVÁK,^{1,2,a} Alexandra KEMÉNY,^{1,2,b} ORBULOV Imre Norbert ORBULOV^{1,2,c}

- ¹ Budapest University of Technology and Economics, Faculty of Mechanical Engineering, Department of Materials Science and Engineering, Budapest, Hungary, szovak.benedek@edu.bme.hu
- ² MTA-BME Lendület High-performance Composite Metal Foams Research Group, Budapest, Hungary
- ^a szovak.benedek@edu.bme.hu, ^b kemeny.alexandra@gpk.bme.hu, ^c orbulov.imre.norbert@gpk.bme.hu

Abstract

Metal foams are cellular materials with outstanding specific mechanical properties, such as high specific energy absorption capacity, owing to its cellular structure. Metal foams are cellular materials with good specific mechanical properties, such as high specific energy absorption, owing to the metal matrix. The aim of this study is to simplify the reinforcement of syntactic metal foams with directional fibres. In previous studies, the fibres were positioned using an external orientation frame. To avoid this, reinforcing material layers in a prefabricated mesh form were placed in the crucible, which is thus perpendicular to the direction of the casting. The fabrication resulted in syntactic metal foam samples reinforced with fibres oriented along two axes.

Keywords: metal foam, syntactic foam, fibre reinforcement.

1. Introduction

Nowadays, there is an increasing demand for materials with low density and high strength. Conventional materials such as metals and ce-ramics cannot always meet these increasingly strict requirements.

The problem can be approached from two different directions: either the density of high-strength materials must be reduced, or the strength of low-density materials must be increased. This can be achieved by using composites, which combine high-strength and low-density materials in such a way that they com-pensate for each other's shortcomings in meeting the requirements while exploiting their advantages.

1.1. Composites

Composites are combination of materials which differ in composition or form on a macro scale. The constituents may retain their identities in the composite. Normally, the constituents can be physically identified, and there is an interface between them [1]. These components are the high-strength reinforcing material, which can absorb the load, and the matrix material which holds the reinforcing material units together, transmitting

the load to them and protecting them from environmental influences.

The bond between the two main constituent parts is of great importance, the strength of the bond that is formed influences the behavior of the composite. A transition layer may be formed, but in many cases the effect is not beneficial for the application [2–4].

In aluminium matrix composites, the effect of different reinforcing materials is investigated, these reinforcing materials can be in the form of grains, fibres, fibre bundles or quilts [5–7]. In the case of fibre reinforcement, it can be short staple fibres, which, due to its random arrangement, has similar effect in all directions as the grains. Or it can be directional fibre reinforcement [8, 9], in this case, the reinforcing material only acts in the direction of the fibre axis, but the reinforcing effect is greater.

1.2. Metal foams

Metal foams are cellular materials with a metallic matrix in which a cellular internal structure is developed to reduce mass [10]. On the basis of the internal porous structure, they can be classified into open-cell foams, in which the internal cells are permeable [11], and closed-cell foams, in

which the individual cells are separated by a solid cell wall [12]. A subgroup of closed-cell foams are syntactic foams, in which the porous structure is formed by the introduction of a filler into the solid matrix [13]. Syntactic foams are considered as composite materials. Owing to their low density, they have brain specific mechanical properties, but they cannot withstand tensile stresses due to their cellular structure.

1.3. Goal of this study

In previous research [14, 15] the possibility of using oriented fibre reinforcement was investigated. In these studies, the reinforcing fibres were placed parallel to the casting direction to increase the tensile strength. However, a complex manufacturing process was required to produce this structure. The goal of this study is to simplify the manufacturing process.

2. Materials

Al99.5 aluminum was used as matrix material due to its low density and high ductility. The exact composition of the alloy was measured with a WAS PMI-MASTER SORT optical spectrometer (Worldwide Analytical Systems AG, Uedem, Germany), the composition is presented in Table 1.

Table 1. Chemical composition of the Al99.5 matrix

Elements	Weight %	
Al	99,5	
Si	0,0293	
Fe	0,335	
Cu	<0,0050	
Mn	<0,0050	
Mg	<0,0010	
Zn	0,0100	
Cr	<0,0050	
Ni	0,0108	
Ti	<0,0010	
Sn	0,0367	

The filler material used was expanded glass beads in the size range of $\emptyset 2.87\pm0.50$ mm, purchased from Stikloporas (Stikloporas UAB, Druskinikai, Lithuania). The reinforcement material used was stainless steel mesh 1.4307 (X2CrNi18-9) with $\emptyset 0.64\pm0.02$ mm fibre diameter, purchased from Jurotissu Kft. (Jurotissu Kft., Budapest, Hungary). The reinforcement and the filler is shown on Fig. 1.

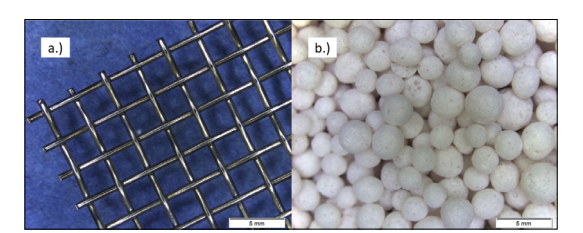


Fig. 1. a) Reinforcing mesh and b.) filler

3. Simplified manufacturing process

The filler and reinforcement were layered in a 60×60×380 mm S235IR steel crucible with a wall thickness of 2 mm. The distance of the mesh pieces used as reinforcing material from each other along the axis of the casting direction was measured on the basis of the filler volume: the theoretical volume of the 10 mm high filler layer was 31.36 ml. This was rounded to 31 ml during construction and measured with a measuring cylinder. After this volume of filler was added, manual vibration was applied to ensure that the surface was perpendicular to the axis of the casting. This was repeated seven times, and then 95 ml (30 mm layer) of filler was placed over the final layer of mesh to create reference samples. The layering steps are shown in Fig. 2.

The prepared charge was also sealed from above with 1.4307 steel mesh to prevent displacement of the filler particles during infiltration. The crucible was heated to 550°C in a Prothermo Hoffmann B-70 box furnace (Prothermo Hoffmann Kft., Kecskemét, Hungary) and held for 1.5 hours. The matrix was heated to 750 °C in an Inductor IF-15 induction melting furnace (Inductor Kft., Diósd, Hungary). The melt temperature was measured with a Maxthermo MD-3003 K thermometer (MAXIMUM ELECTRONIC CO., LTD., Taipei Hsien). The molten matrix was poured into the crucible,

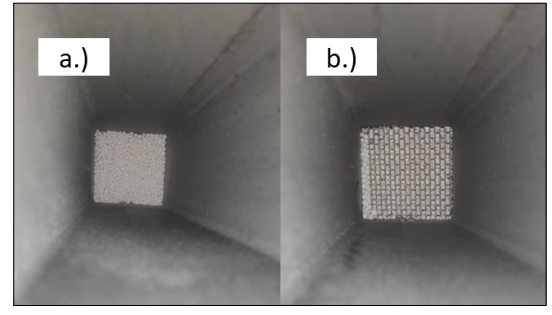


Fig. 2. Placement of a.) filler and b.) reinforcement in the crucible.

and infiltration was performed using 400 kPa (4 bar) argon gas pressure. The crucible was allowed to cool to room temperature in the open air.

Samples were taken from the block, some of which were ground and polished with a diamond suspension of 1 μ m grain size for microscopic examination.

4. Results

Density was determined from geometric dimensions and mass. The value was 1.63±0.06 g/cm³ for the reinforced specimens and 1.26±0.01 g/cm³ for the reference specimens without reinforcing fibres. The use of reinforcing fibres increased the density by 23%.

The structure of the sample is shown on Fig. 3. The spacing of the reinforcing mesh layers placed was determined by stereomicroscopy between the fibres closest to each other along the axis of the casting, as shown in Fig. 4. The average distance between the fibres is 9.55±0.55 mm. This

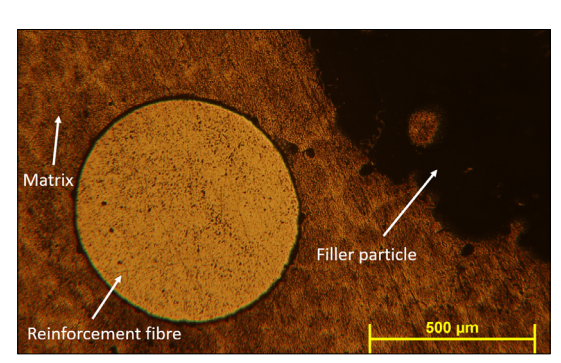


Fig. 3. Metal microscopy image of the structure of mesh reinforced syntactic metal foam.

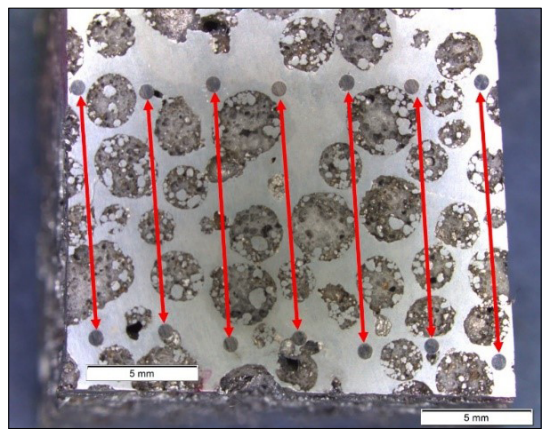


Fig. 4. Illustration of the distance between reinforcement layers in the cross section.

deviation from the intended distance of 10 mm is due to rounding, inaccuracies in the measurement of the filler volume, and better compaction due to the larger surface area of the crucible.

5. Conclusions

The following conclusions were drawn from the study:

- Low pressure infiltration (400 kPa) is a suitable process for the production of syntactic metal foams with oriented fibre reinforcement;
- The process used significantly simplifies the manufacturing process compared to methods used in previous research:
- the structure obtained is worthy of further testing, in particular to study the tensile and compressive properties;
- the use of the prefabricated mesh as reinforcing material deserves further testing for larger pieces with fiber orientation parallel to the casting direction to study tensile and bending properties.

Acknowledgements

This publication was supported by the EKÖP-24-3-BME-4 University Researcher Scholarship Program of the Ministry for Culture and Innovation from the source of the National Research, Development and Innovation Fund.

This work was supported by the National Research, Development and Innovation Office (NKFIH), under grant agreement OTKA-FK 21 138505.

References

- [1] ISO 21347:2005 Space systems Fracture and damage control, 2005.
- [2] Kumar N., Chittappa H. C., Ezhil Vannan S.: Development of Aluminium-Nickel Coated Short Carbon Fiber Metal Matrix Composites. Materials Today: Proceedings, 5. (2018) 11336–11345. https://doi.org/10.1016/j.matpr.2018.02.100.
- [3] Máté P., Szekrényes A.: The Effect of the Layup on the Stability of Composite Cylindrical Shells. Periodica Polytechnica Mechanical Engineering, 68/4. (2024) 291–303. https://doi.org/10.3311/PPme.23424.
- [4] Kun K., Bata A., Ronkay F.: Investigation of the Replication Quality of Microstructures on Injection Moulded Specimens Made from Recycled Polypropylene Composites Reinforced with Carbon Nanotubes. Periodica Polytechnica Mechanical Engineering, 68/3. (2024) 247–53. https://doi.org/10.3311/PPme.37288.
- [5] Zaiemyekeh Z., Liaghat G. H., Ahmadi H., Khan M. K., Razmkhah O.: Effect of strain rate on de-

- formation behavior of aluminum matrix composites with Al 2 O 3 nanoparticles. Materials Science & Engineering A 753. (2019) 276–284. https://doi.org/10.1016/j.msea.2019.03.052.
- [6] Vijayaram T. R., Sulaiman S., Hamouda A. M. S., Ahmad M. H. M.: Fabrication of fiber reinforced metal matrix composites by squeeze casting technology. Journal of Materials Processing Technology, 178. (2006) 34–8. https://doi.org/10.1016/j.jmatprotec.2005.09.026.
- [7] Bedmar J., Torres B., Rams J.: Manufacturing of Aluminum Matrix Composites Reinforced with Carbon Fiber Fabrics by High Pressure Die Casting. Materials, 15. (2022) https://doi.org/10.3390/ma15093400.
- [8] Zhao H., Yuan T., Zeng C., Peng W., Sun Z., Hu H.: Microstructure and mechanical properties of steel wire reinforced Mg matrix composites fabricated by composite extrusion. Composites Communications, 43. (2023) 101711. https://doi.org/10.1016/j.coco.2023.101711.
- [9] Almeida J. H. S., Miettinen A., Léonard F., Falzon B. G., Withers P. J.: Microstructure and damage evolution in short carbon fibre 3D-printed composites during tensile straining. Composites Part B, 292. (2025) 112073. https://doi.org/10.1016/j.compositesb.2024.112073.
- [10] Marx J., Rabiei A.: Overview of Composite Metal Foams and Their Properties and Performance. Advanced Engineering Materials, 19. (2017) 1–13.

- https://doi.org/10.1002/adem.201600776.
- [11] Johnson Q. C., Kenesei P., Petruzza S., Plumb J., Sharma H., Park J. S. és mtsai.: Mapping 3D grain and precipitate structure during in situ mechanical testing of open-cell metal foam using micro-computed tomography and high-energy X-ray diffraction microscopy. Materials Characterization, 195. (2023) 112477. https://doi.org/10.1016/j.matchar.2022.112477.
- [12] Naeem M. A., Gábora A., Mankovits T.: Influence of the manufacturing parameters on the compressive properties of closed cell aluminum foams. Periodica Polytechnica Mechanical Engineering, 64. (2020) 172–8. https://doi.org/10.3311/PPME.16195.
- [13] Kincses D. B., Károly D., Bukor C.: Production and testing of syntactic metal foams with graded filler volume. Materials Today: Proceedings, 45. (2020) 4225–4228. https://doi.org/10.1016/j.matpr.2020.12.163.
- [14] Szovák B., Maróti J. E., Kemény A., Orbulov I. N.: Unidirectional fibre reinforcement of syntactic metal foams. IOP Conference Series: Materials Science and Engineering, 1313. (2024). https://doi.org/10.1088/1757-899X/1313/1/012005.
- [15] Szovák B., Kemény A., Orbulov I. N.: Unidirectional steel wire reinforced metal matrix syntactic foams. IOP Conference Series: Materials Science and Engineering, 1319. (2024). https://doi.org/10.1088/1757-899X/1319/1/012007.



Acta Materialia Transylvanica 8/1. (2025) 47–50.

DOI: Hungarian: https://doi.org/10.33923/amt-2025-01-10

English: https://doi.org/10.33924/amt-2025-01-10



Effect of Welding Pressure During Ultrasonic Welding Between Nickel-Plated Copper and Aluminium Sheets

Alam Md ZAMIUL, 1 Márton SCHRAMKÓ, 2 Tünde Anna KOVÁCS3

- ¹ Óbuda University, Bánki Donát Faculty of Mechanical and Safety Engineering, Budapest, Hungary, zamiulalam22@stud.uni-obuda.hu
- ² Óbuda University, Doctoral School on Materials Sciences and Technologies, Budapest, Hungary, schramko.marton@bgk.uni-obuda.hu
- ³ Óbuda University, Bánki Donát Faculty of Mechanical and Safety Engineering, Budapest, Hungary, kovacs.tunde@bgk.uni-obuda.hu

Abstract

This study investigates the effect of welding pressure on ultrasonic welding of aluminium sheet and nickel-plated copper sheet. Both specimens were $60\times10\times0.5$ mm in size with a 10 mm overlap and the coating thickness was 8–12 μ m. The experiment was performed at different welding pressures from 0.14 MPa to 0.31 MPa while maintaining constant welding energy, time and amplitude. The results showed that the highest tensile strength of 380 N was achieved at a welding pressure of 0.14 MPa, while higher pressures caused a decrease in the tensile strength, which is believed to be due to internal cracks and hardening. To achieve the strongest bond, the optimal welding pressure was determined to be 0.14 MPa.

Keywords: ultrasonic welding, welding pressure, tensile strength, welding defects, plated copper.

1. Introduction

Ultrasonic welding was first developed in the mid-20th century, initially as a way to improve upon the process of spot welding in the aerospace industry. Still, it was not until the 1960s that practical uses for rigid plastics emerged. The process of ultrasonic welding for thermoplastics was established. Ultrasonic welding was accidentally discovered in 1963 by Robert Soloff, founder of Sonics & Materials Inc., who managed to weld a plastic tape dispenser with an ultrasonic probe. In 1965, Soloff, with his collaborator Seymour Linsley, received a patent for this method, helping to establish a key milestone in the development of the technology. Soloff developed the first ultrasonic welding machine, and he adapted a drill press to create the first automated ultrasonic welder, which was initially used in the toy indus-

Ultrasonic welding is a solid-state welding process that uses high-frequency ultrasonic vibrations to join materials, primarily metals and plastics, and does not require heat, filler metal, or adhesives. It works by using the vibrations combined with the applied welding pressure on the materials. This can be used to weld dissimilar materials like aluminium and copper because it is eco-friendly, reliable, and fast, whereas the fusion welding methods are not suitable [2–4].

Ultrasonic welding equipment operates in a frequency range of 15 kHz to 70 kHz. Typically, for thinner materials, higher sound frequencies are applied, and lower frequencies are applied for thicker materials [4].

Ultrasonic waves can modify the mechanical properties of the welds (hardness and tensile strength) by modifying the dislocation density. However, to improve the above-mentioned properties, the performance of ultrasonic welding must be optimized. When welding aluminium-copper joints, the right parameter selection for the right compression, amplitude, and energy is crucial to achieve high-quality welds. The process can be divided into 4 main groups according to ISO 4063, based on which material group is welded and how. In addition, the process can be divided into two main types based on the process execution: spot welding and continuous welding,

which are used for specific applications depending on the size and complexity of the part. Spot welding is simpler and can be used for small parts, while continuous welding is used for large and complex workpieces [3, 5].

Ultrasonic welding is used in many industries because of its high efficiency and versatility. It is widely used in the automotive industry to join components like electrical connectors and wire harnesses, and provides a quick and heat-free solution. In the electronics industry, it is used to join microcircuits and semiconductor components with minimal damage to the sensitive components. In the medical industry, it is used for airtight packaging and sealing for the sterility and integrity of medical products. Additionally, it is used in packaging to create blister packs and provide a tamper-resistant closure. This welding is also notable in aerospace applications to join composite structures and thermoplastic composites to enhance strength-to-weight ratios. Moreover, its ability to join dissimilar materials determines more possibilities in product design and customization across industries [6, 7].

Ultrasonic welding has many advantages over other welding methods, such as welding different materials like pure or coated aluminium and copper. For Al-Cu joints, it makes a solid-state bond, which is perfect for making lithium-ion battery packs because it will join more conductive materials with low heating. For plastics, ultrasonic welding utilizes high-frequency sound waves to melt and bond; this process is very clean and effective, with very little thermal damage [7–11].



Fig. 1. Ultrasonic welding machine.

2. Materials and methodology

This experiment investigates the effect of welding pressure on the ultrasonic welding of Al and Ni-coated Cu. Ultrasonic welding was used for the welding of these two dissimilar materials because it can create strong bonds without generating excessive heat, which can cause damage to certain materials

Shakil et al. made several tests to determine the optimal ultrasonic welding parameters. They used aluminium alloy and stainless steel for the experiment and declared that a higher welding pressure requires a shorter welding time and lower energy than in the case of lower welding pressure to earn the same tensile load. Based on the literature results, we built the experiments [12].

The experiment was performed by varying the welding pressure between 0.14 and 0.31 MPa in increments of 0.035 MPa, keeping the welding energy, time, and amplitude constant. The welding energy was 100 J, the welding time was 1.20 seconds, and the applied amplitude was 45 μm . Both the aluminium and nickel-coated copper samples were 60 mm long, 10 mm wide, and 0.5 mm thick, with an overlap of 10 mm, resulting in an overlap area of 100 mm². The nickel coating had an average thickness of 8-12 μm .

To perform the test, a Branson (Ultraweld L20) ultrasonic welding machine (see Fig. 1) was used to create the sample welds, and a tensile testing machine was used for the tests.

Welding pressure variation is crucial in this experiment because it affects the strength and quality of the weld.

Overall, the experiment was intended to determine the impact of welding pressure on the ultrasonic welding process of Al and Ni-coated Cu by employing a controlled setup and constant parameters.

3. Results

3.1. Effect of welding pressure on breaking force

The development of the tensile strength during ultrasonic welding of Al- and Ni-coated Cu was analyzed as a function of the welding pressure, as shown in the welding pressure-tensile strength curve (Fig. 2). The welding pressure was varied between 0.14 MPa and 0.31 MPa, and the tensile strength was measured as the average of three samples at each welding pressure level.

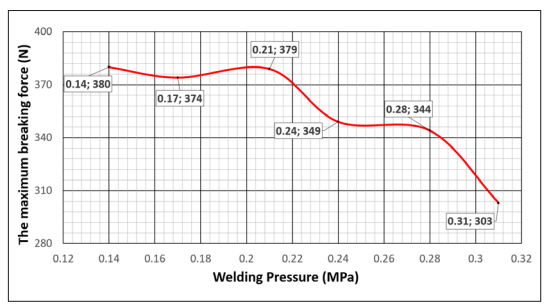


Fig. 2. Diagram of the required breaking force and the welding pressure.

The figure shows that the highest tensile strength was achieved at the lowest welding pressure tested, 0.14 MPa, with a tensile strength of 380 N. Although it drops slightly at 0.17 MPa to 374 N, the general trend shows a continuous decrease in tensile strength as the welding pressure increases. The lowest tensile strength is found at 0.31 MPa, where the force value is 303 N.

These results suggest that higher welding pressure negatively affects weld strength, probably due to material deformation or damage. The optimal welding pressure in terms of tensile strength in this experiment was 0.14 MPa, which resulted in the highest tensile strength of 380 N under the experimental conditions.

3.2. Effect of Welding Pressure on Fraction Location

Analysis of the fracture location showed that the welding pressure adversely affects the integrity of the joint if nothing else is modified. Fig. 3 lshows that the aluminium sheet in the pieces welded at 0.14 MPa broke during the tensile test, indicating that the strength of the joint is higher than that of the aluminium. In the pieces welded at 0.31 MPa, shown in Fig. 4 the weld joint broke, indicating a deterioration in the strength of the joint due to excessive welding pressure.

The figures correlate with the tensile strength measurements, confirming that when the welding pressure is at 0.14 MPa, the bond breaks in the base material, indicating a strong bond. Excessive welding pressure is not suitable for forming a proper bond, as the location of the break occurs within or very close to the bond. For strong bonds, the base material typically breaks, while in the case of incorrect parameters, the break may occur in the immediate vicinity of the weld or in the weld. This suggests that in the case of incorrect parameters, the bond forms a weak connection. In the surroundings of the welding area,



Fig. 3. Samples welded at lower pressure.

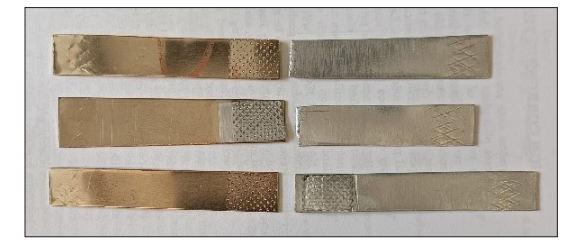


Fig. 4. Samples welded at higher pressure.

the likelihood of cracks and dislocation density increases, which lowers the load-bearing capacity of the bond after welding. Therefore, 0.14 MPa is the optimal welding pressure to achieve the appropriate strength among the tested parameters.

4. Conclusion

In this study, the welding pressure is investigated while keeping other factors constant. The results show that the highest tensile strength, 380 N, is achieved at a pressure of 0.14 MPa. At higher welding pressures, the tensile strength decreases, and the minimum value of the tensile strength is 303 N, which is achieved at the highest welding pressure of 0.31 MPa. After this, the weld has a much lower probability of forming a strong joint. This suggests that in our case, increasing the welding pressure degrades the weld quality above a certain point, so the correct parameter selection is very important during welding. Incorrect parameters can easily lead to cracks or internal damage in the weld. Analysis of the fracture location suggests that higher welding pressure reduces the load-bearing capacity of the specimen.

Future implementations based on this study could focus on process optimization of ultrasonic welding by studying other parameters such as welding energy, time, and amplitude. Further studies could include varying material thickness, joint size, and the effect of varying ultrasonic frequencies. In addition, investigating the effects of different types of coatings and surface treatments could provide valuable information for joint testing and material compatibility in ultrasonic welding.

References

- [1] Woo J.: A short History of the development of Ultrasound in Obstetrics and Gynecology. http://www.ob-ultrasound.net/curie.html (letöltve: 2025. április 1.)
- [2] Fujii H. T., Goto Y., Sato Y. S., Kokawa H.: Microstructure and lap shear strength of the weld interface in ultrasonic welding of Al alloy to stainless steel. Scripta Materialia, 116. (2016) 135–138. https://doi.org/10.1016/j.scriptamat.2016.02.004
- [3] Tang M., Zhang P., Yu Z., Shi H., Li S., Wu D., Tian, Y.: Study on ultrasound welding process of aluminum/copper dissimilar metals. Physics of Metals and Metallography, 121/14. (2020) 1400–1410. https://doi.org/10.1134/S0031918X20140173
- [4] de Leon M., Shin H. S.: Review of the advancements in aluminum and copper ultrasonic welding in electric vehicles and superconductor applications. Journal of Materials Processing Technology, 307. (2022) 117691. https://doi.org/10.1016/j.jmatprotec.2022.117691
- [5] Yin P., Xu C., Pan Q., Zhang W., Jiang X.: Effect of different ultrasonic power on the properties of RHA steel welded joints. Materials, 15/3. (2022) 768.
 - https://doi.org/10.3390/ma15030768
- [6] Abbas Z., Zhao L., Deng J., Wang S., Hong W.: Advances in ultrasonic welding of lightweight alloys: A review. High Temperature Materials and Processes, 42/1. (2023) 20220298. https://doi.org/10.1515/htmp-2022-0298
- [7] Bhudolia S. K., Gohel G., Leong K. F., Islam A.: Advances in ultrasonic welding of thermoplastic composites: a review. Materials, 13/6. (2020) 1284. https://doi.org/10.1515/htmp-2022-0298

- [8] Das S., Satpathy M. P., Routara B. C., Nanda B. K., Sahoo S. K.: Ultrasonic metal welding of Al/Cu joints with Ni coating: parametric effects on joint performance and microstructural modifications. International Journal of Materials Research, 115/11–12. (2024) 1105-1115. https://doi.org/10.1515/jimr-2024-0068
- [9] Li J., Zillner J., Balle, F.: In-depth evaluation of ultrasonically welded Al/Cu joint: Plastic deformation, microstructural evolution, and correlation with mechanical properties. Materials, 16/8. (2023) 3033. https://doi.org/10.3390/ma16083033
- [10] Bose S., Chelladurai H. M., Kanaiyaram P.: An experimental investigation on feasibility of submerged ultrasonic spot welding of thermoplastics. Proceedings of the Institution of Mechanical Engineers, Part L. Journal of Materials: Design and Applications, 238/10. (2024) 2043–2057. https://doi.org/10.1177/14644207241239475
- [11] Görick D., Welsch J., Gerardo C. D., Kupke M., Cretu E., Rohling R.: Inline Monitoring of continous Ultrasonic Welding Processes of Thermoplastic Composites via a custom polyCMUT based Ultrasound Array. In: 20th World Conference on Non-Destructive Testing (WCNDT) 29(6). 2024. NDT. net. https://doi.org/10.58286/29933
- [12] Shakil M., Tariq N. H., Ahmad M., Choudhary M. A., Akhter J. I., Babu S. S.: Effect of ultrasonic welding parameters on microstructure and mechanical properties of dissimilar joints. Materials & Design, 55. (2014) 263–273. https://doi.org/10.1016/j.matdes.2013.09.074